Proposal to PAC 50

Precision Measurement of the Neutral Pion Transition Form Factor

A. Afanasev[1], M. Amaryan[2], A. Asaturyan[3], T. Black[3], W.K. Brooks[4], J. Burggraf[5], V. Burkert[6], R. Capobianco[7], D.S. Dale[†8], S. Diehl[16,7], D. Dutta[†9], A. Fabrizi[10], T. Forest[8], L. Gan[†3], S. Gevorkyan[12], T. Hayward[7], K. Joo[7], G. Kainth[7], A. Kim[7], V. Klimenko[7], V. Kubarovsky[6], I. Larin[†*10], L. Lasig[7], D. McNulty[8], R. Miskimen[†10], E. Pasyuk[†6], C. Peng[14], J. Richards[7], J. Ritman[15], R. Santos[7], S. Schadmand[15], A. Schick[10], S. Srednyak[11], U. Shrestha[7], P. Simmerling[7], S. Stepanyan[6], I. Strakovsky[1], N. Trotta[7], and G. Turnberg[10]

[1]The George Washington University, Washington, DC 20052
[2]Old Dominion University, Norfolk, VA 23529
[3]University of North Carolina Wilmington, Wilmington, NC 28403
[4]Universidad Técnica Federico Santa María, Casilla 110-V Valparaíso, Chile
[5]Lawrence Livermore National Laboratory, Livermore, CA 94550
[6]Thomas Jefferson National Accelerator Facility, Newport News, VA 23606
[7]University of Connecticut, Storrs, Connecticut 06269, USA
[8]Idaho State University, Pocatello, ID 83209
[9]Mississippi State University, Mississippi State, MS 39762
[10]University of Massachusetts, Amherst MA 01003
[11]Duke University, Durham, NC 27708
[12]Joint Institute for Nuclear Research, Dubna, Russia 141980
[14]Argonne National Lab, Lemont, IL 60439
[15]GSI Helmholtzzentrum für Schwerionenforschung GmbH, D-64291 Darmstadt, Germany
[16]II Physikalisches Institut der Universitaet Giessen, 35392 Giessen, Germany

June 22, 2022

*Contact person
†spokesperson

Abstract

We propose a measurement of the π^0 space-like transition form factor (TFF) through the Primakoff reaction with virtual incident photons. The experiment will run using the PRad setup in Hall B using a 250 μm thick silicon target, and a 10.5 GeV electron beam with 10 nA current. The measurement has sensitivity to two fundamental observables in low-energy, strong-interaction physics, (i) the π^0 radiative decay width $\Gamma_{\pi^0\to\gamma\gamma}$, predicted by the chiral anomaly, and (ii) the π^0 electromagnetic transition radius. The measurement will determine $\Gamma_{\pi^0\to\gamma\gamma}$ with an estimated uncertainty of $\pm\,0.7(1.4)\,\%$ stat (sys), to be compared with the combined PrimEx-I and PrimEx-II result of $\pm\,0.7(1.3)\,\%$ [1], and the π^0 electromagnetic transition radius with an estimated uncertainty of $\pm 3\,\%$, to be compared with the PDG average of $\pm 5\,\%$. One of the largest uncertainties in the Standard Model prediction for the muon anomalous magnetic moment is hadronic light-by-light scattering, which critically depends on knowledge of the pseudo-scalar meson TFFs in the low-Q^2 region. By measuring the π^0 TFF over the region $Q^2 \approx .003$ to $0.3\,\mathrm{GeV}^2$ where no data currently exists, the proposed experiment will constrain approximately 65 % of the pseudo-scalar pole contribution to HLbL with an estimated uncertainty of $\pm 6\,\%$.

Contents

1 Executive Summary

We request 67 PAC days to perform the measurement of the neutral pion transition form factor (TFF) in the low-Q^2 space-like region using the magnetic-spectrometer-free PRad setup [2] in Hall-B with its data acquisition upgraded with the JLab fADC system. The experiment will use 10.5 GeV CW electron beam, with a current of 10 nA, on a 250 μm thick silicon plate placed in front of the PRad setup. The measurement will be performed through the Primakoff reaction with a virtual incident photon beam. Both the scattered electron and the two photons from π^0 decay will be detected in the hybrid electromagnetic calorimeter HYCAL, with GEM detectors from the PRad experiment used for electron tracking and vetoing charged background. It will allow us to determine two key observables in low-energy strong-interaction physics, (i) the neutral pion radiative width $\Gamma_{\pi^0\to\gamma\gamma}$, predicted by the chiral anomaly, and (ii) the neutral pion transition radius. Measurements of the neutral pion TFF are also very important in constraining and allowing for calculations of the hadronic light-by-light (HLbL) scattering contribution to the muon anomalous magnetic moment. The proposed measurement has sensitivity to the TFF over a heretofore unmeasured Q^2 range of $0.003\,\mathrm{GeV}^2$ to $0.3\ \mathrm{GeV}^2$ (as shown in Fig. 42), allowing a clean determination of the slope and curvature parameters in the TFF, and complementing the space-like BESIII [3], CELLO [4] and CLEO [5] measurements at $Q^2 > 0.3\,\mathrm{GeV}^2$, and Dalitz decay measurements in the time-like region [6, 7, 8, 9, 10, 11].

The $\Gamma_{\pi^0\to\gamma\gamma}$ extraction procedure and experimental setup are very similar to the PrimEx photo-production measurement [1]. Relative to PrimEx, we expect an improvement in the largest contributions to the total PrimEx systematic error: beam flux (measurements of electron beam flux have better precision than photon beam flux), and beam background (the PRad vacuum chamber eliminates downstream beam interactions, the main non-resonant background for Primakoff photo-production in PrimEx).

The proposed experiment will:

- Measure the $\Gamma_{\pi^0\to\gamma\gamma}$ with an uncertainty of 1.4% or better.
- Measure the neutral pion TFF with unprecedented precision, over an as yet unexplored Q^2 range of $0.003\,\mathrm{GeV}^2$ to $0.3\ \mathrm{GeV}^2$.
- Measure the TFF slope and curvature parameters a_π and b_π with projected statistical uncertainties of approximately 6% and 17% respectively.
- Measure the neutral pion electromagnetic transition radius with an uncertainty of 3%.
- Constrain the pion-pole contribution to HLbL (the largest contribution) with an uncertainty of 6 %.

2 Introduction and physics motivation

Measurements of the neutral pion transition form factor (TFF) in the low-Q^2 space-like region can determine two key observables in low-energy strong-interaction physics, the neutral pion radiative width $\Gamma_{\pi^0\to\gamma\gamma}$, and the neutral pion transition radius. These observables provide important test points for calculations based on fundamental symmetries and chiral perturbation theory, [12], as well as providing important constraints for hadronic corrections to the muon anomalous magnetic moment [13, 14].

Primakoff π^0 electro-production can be used to measure the space-like π^0 electromagnetic TFF. Fig. 1 shows the Feynman diagram for the interaction vertex. We define Q_1^2 as the negative 4-momentum transfer squared from the electron vertex, and Q_2^2 as the corresponding quantity from the nuclear vertex, where $Q_2^2 = -t$ in terms of the usual Mandelstam variable.

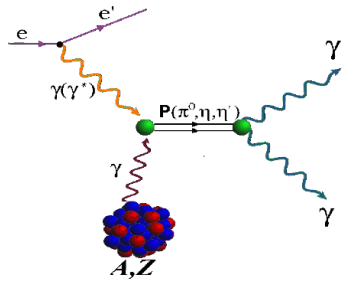

Figure 1: Feynman diagram for the virtual Primakoff reaction

The transition is characterized by the form factor $F_{\gamma^*\gamma^*\to\pi^0}(-Q_1^2,-Q_2^2)$, which to order $O(Q^4)$ is given by,

$$F_{\gamma^*\gamma^*\to\pi^0}(-Q_1^2,-Q_2^2) = \sqrt{\frac{4\Gamma_{\pi^0\to\gamma\gamma}}{\pi\alpha^2 m_\pi^3}}\left[1-\frac{a_\pi}{m_\pi^2}\left(Q_1^2+Q_2^2\right)+\frac{b_\pi}{m_\pi^4}\left(Q_1^4+Q_2^4\right)+\frac{c_\pi}{m_\pi^4}Q_1^2Q_2^2+...\right] \quad (1)$$

where a_π and b_π are the linear and curvature terms in the TFF, respectively, and c_π is a cross term in the expansion. The connection with the π^0 mean square electromagnetic transition radius is given by,

$$< r^2 >_{\pi^0} = 6\frac{a_\pi}{m_\pi^2} \quad (2)$$

The cross section for virtual Primakoff production has been given by Hadjimichael and Fallieros [15],

$$\frac{d^3\sigma_P}{dE_2 d\Omega_2 d\Omega_\pi} = \frac{Z^2\eta^2}{\pi}\sigma_M \frac{k_\pi^4}{t^2}\frac{\beta_\pi^{-1}}{E_\pi}\left|F_N(t)\right|^2 \left|\frac{F_{\gamma^*\gamma^*\to\pi^o}(-Q^2,t)}{F_{\gamma^*\gamma^*\to\pi^o}(0,0)}\right|^2 sin^2(\frac{\theta_e}{2})sin^2(\theta_\pi) \times \left[4E_1E_2sin^2\phi_\pi + |\vec{q}|^2/cos^2(\frac{\theta_e}{2})\right] \quad (3)$$

where σ_M is the Mott cross section ,

$$\sigma_M = \frac{\alpha^2 cos^2(\frac{\theta_e}{2})}{4E_1^2 sin^4(\frac{\theta_e}{2})} \quad (4)$$

with η^2 given by

$$\eta^2 = \frac{4}{\pi m_\pi^3}\Gamma_{\pi^0\to\gamma\gamma} \quad (5)$$

In Eqn. 3 $F_N(t)$ is the nuclear electromagnetic form factor, θ_e is the electron scattering angle, k_π is the pion momentum, and θ_π is the angle between the virtual photon direction $\vec{q}$ and the neutral pion direction $\vec{k}_\pi$. This expression for the cross section in similar to that for the real Primakoff effect, with the notable exception of the form factor $F_{\gamma^*\gamma^*\to\pi^0}(-Q^2,t)$ which is of interest here. An earlier formalism for the electroproduction cross section by Donnelly and Cotanch [16] also exists. We have verified that the virtual Primakoff cross section given in Eqn. 3 by Hadjimichael and Fallieros is equivalent to this alternate form.

The $\gamma^*\gamma^*\pi^0$ vertex has been studied theoretically in VMD and ChPT based models, [17, 18, 19], as well as those based on treatments of quark substructure [20, 21, 22]. In light of the recent result for muon $g-2$, there has been considerable theoretical interest in the pseudo-scalar TFFs and how they impact hadronic corrections to $(g-2)_\mu$ (see discussion in section 3). Most recently lattice calculations [23, 24] have been developed with sufficient accuracy to complement and test predictions for hadronic corrections to $(g-2)_\mu$ based on analytical approaches.

The most significant background to consider in Primakoff experiments is π^0 coherent photo-production [1]. Fig. 2 shows an example of this from the PrimEx-II ^{28}Si data. The prominent peak at lowest angle is Primakoff production, and the peak at $\approx 1.3^\circ$ is nuclear coherent production. The methodology for extracting the Primakoff signal from the coherent and incoherent backgrounds is well established [1]. Stated briefly, shapes of the Primakoff and coherent angular distributions are constrained, the former by QED and the nuclear electromagnetic form factor, and the latter by the t-dependence of the strong nuclear form factor and the pion-nucleus interaction. Therefore, the analysis effectively reduces to fitting the π^0 angular distribution with the squared sum of Primakoff and coherent amplitudes, with the coherent amplitude multiplied by an arbitrary complex phase. The complex phase accounts for the phase difference between the Coulomb amplitude (Primakoff), and the strong amplitude (coherent).

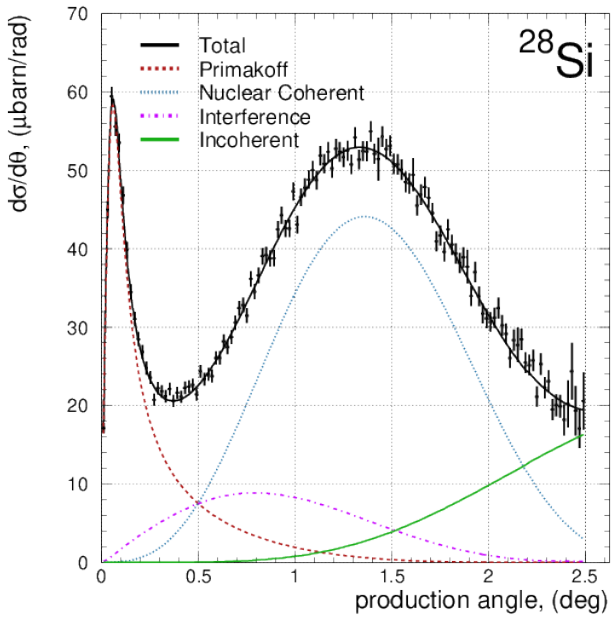

Figure 2: ^{28}Si data from the PrimEx-II analysis. The curves show the Primakoff signal (brown), and the coherent (blue), interference (magenta) and incoherent (green) backgrounds.

S. Gevorkyan, our PrimEx theoretical collaborator, has developed a generalization of the coherent amplitude for the case of electro-production. Details of the calculation are given in Appendix A. For the TFF measurement we plan to take data on a ^{28}Si target, which will allow us to capitalize on the theoretical effort invested by PrimEx in the calculation of coherent and incoherent reactions on ^{28}Si. In the low-Q^2 range of the proposed TFF measurement the photo-production and electro-production coherent angular distributions are similar in shape.

Finally, we note that a proposal to measure the pseudo-scalar TFFs was developed by the PrimEx Collaboration over 20 years ago. The proposal was included in the original JLab white paper as a key experiment driving the 12 GeV energy upgrade [25, 26].

3 Hadronic corrections to the muon anomalous magnetic moment: HLbL

Recently there has been considerable interest in measurements of the pseudo-scalar meson TFFs as a means to constrain hadronic corrections to the muon anomalous magnetic moment [14]. Defining $a_\mu = (g-2)_\mu/2$ as the deviation of the magnetic moment from the

value g=2 for a point-like spin-1/2 Dirac particle, the experimental measurement [27] and Standard Model (SM) prediction [14] for a_μ are given by,

$$a_\mu^{exp} = 116\ 592\ 061\ (41) \times 10^{-11} \tag{6}$$

$$a_\mu^{SM} = 116\ 591\ 810\ (43) \times 10^{-11} \tag{7}$$

which gives a 4.2σ deviation between experiment and Standard Model. As of this writing FNAL E989 continues to take data on $(g-2)_\mu$, and data taking is planned at J-PARC in the near future. Therefore, we can expect a significant reduction in the experimental error in a_μ over the next several years. For this reason comprehensive theoretical *and experimental efforts* are underway to reduce the Standard Model uncertainty in a_μ.

There are four classes of corrections to the SM prediction for a_μ^{SM}: (i) higher-level QED diagrams to order α^{12}, (ii) electro-weak corrections at 3-loop level, (iii) hadronic vacuum polarization, and (iv) hadronic light-by-light scattering. Theoretical uncertainties in the first two processes, QED and electro-weak corrections, are understood to be small, $\pm 1 \times 10^{-12}$ and $\pm 1 \times 10^{-11}$, respectively, and do not limit the interpretation of the experimental results [14].

The third class of correction, hadronic vacuum polarization HVP, can be calculated using data driven techniques using experimental data. In the data-driven approach the lowest order HVP is given by $\int K(s)R(s)/s^2\ ds$, where $\sqrt{s}$ is the C.M. energy of the e^+e^- system, K(s) is a known kinematic factor, and R(s) is given by,

$$R(s) = \frac{\sigma(e^+e^- \to hadrons)}{\sigma(e^+e^- \to \mu^+\mu^-)} \tag{8}$$

The evaluation of HVP currently stands at $a_\mu^{HVP} = 6845 \pm 40 \times 10^{-11}$ [14]. As new measurements of $e^+e^- \to X$ improve on the determination of R, the error in HVP is expected to significantly decrease.

The fourth class of correction, and arguably the most model-dependent in its evaluation, is hadronic light-by-light scattering, HLbL. Since HLbL is suppressed by a factor of α_{EM} relative to HVP, a_μ^{HLbL} is roughly two orders of magnitude smaller than a_μ^{HVP}. Unlike HVP, HLbL cannot be reduced to purely data-driven forms and must be evaluated using experimental data and hadronic models [13, 14]. The evaluation of HLbL currently stands at $a_\mu^{HLbL} = 92 \pm 19 \times 10^{-11}$ [14]. *Estimated uncertainties in HLbL and HVP are both at the level of* $\approx 30 \times 10^{-11}$.

The single largest contribution to HLbL is from the coupling of two space-like photons to the pseudo-scalar mesons π^0, η and η', with the coupling parameterized by the pseudo-scalar TFFs. TFF data are used as input for the evaluation of the pseudo-scalar pole contribution to HLbL, and for the validation of hadronic models used to calculate the TFFs. Evaluation of the pseudo-scalar pole contribution to HLbL currently stands at

$a_\mu^{HLbL-pole} = 93.8 \pm 4.0 \times 10^{-11}$ [14], and equal to the summed total for HLbL. Due to the low mass of the π^0 relative to the η and η', approximately 67% of $a_\mu^{HLbL-pole}$ comes from the π^0-pole.

Details for calculating $a_\mu^{HLbL-pole}$ are presented in Appendix B. Also presented in the appendix are the computational tools we've used in evaluating $a_\mu^{HLbL-\pi^0}$ for this proposal. $a_\mu^{HLbL-\pi^0}$ is given by the following equations, [28]

$$a_\mu^{HLbL-\pi^0} = \left(\frac{\alpha}{\pi}\right)\left[a_\mu^{\mathrm{HLbL}:\pi^0(1)} + a_\mu^{\mathrm{HLbL}:\pi^0(2)}\right] \tag{9}$$

where the two terms on the right must be evaluated from triple integrals over the TFFs,

$$a_\mu^{\mathrm{HLbL}:\pi^0(1)} = \int_0^\infty dQ_1 \int_0^\infty dQ_2 \int_{-1}^1 d\tau w_1(Q_1,Q_2,\tau)\mathcal{F}_{\pi^0\gamma^*\gamma^*}(-Q_1^2,-(Q_1{+}Q_2)^2)\mathcal{F}_{\pi^0\gamma^*\gamma^*}(-Q_2^2,0) \tag{10}$$

$$a_\mu^{\mathrm{HLbL}:\pi^0(2)} = \int_0^\infty dQ_1 \int_0^\infty dQ_2 \int_{-1}^1 d\tau w_2(Q_1,Q_2,\tau)\mathcal{F}_{\pi^0\gamma^*\gamma^*}(-Q_1^2,-Q_2^2)\mathcal{F}_{\pi^0\gamma^*\gamma^*}(-(Q_1{+}Q_2)^2,0) \tag{11}$$

with $Q_1 = \sqrt{Q_1^2}$ and $Q_2 = \sqrt{Q_2^2}$, and weighting functions w_1 and w_2 given in Appendix B.

The TFF used for our studies is the "LMD+V" form factor (Lowest Meson Dominance + Vector meson), which is almost universally used in calculations of $a_\mu^{HLbL-pole}$ [28]. The LMD+V TFF is the minimal hadronic approximation to Green's functions in the large-N_c limit of QCD, while also satisfying the necessary Brodsky-Lepage behaviour at high Q^2,

$$\lim_{Q^2\to\infty} F_{\gamma^*\gamma^*\to\pi^0}(-Q^2,0) = -\frac{2F_\pi}{Q^2} + O\Big(\frac{1}{Q^4}\Big) \tag{12}$$

The LMD+V TFF is presented in Eqn. 20 of Appendix B.

Fig. 3 shows a plot of $a_\mu^{HLbL-\pi^0}$ as a fraction of the asymptotic limit versus the momentum cutoff in Eqns. 10 and 11. The figure shows that $a_\mu^{HLbL-\pi^0}$ saturates with increasing momentum, and at a cutoff of $Q_{1,2} = 0.55$ GeV, corresponding to $Q^2 = 0.3\,GeV^2$, $a_\mu^{HLbL-\pi^0}$ reaches 65 % of its asymptotic limit.

4 Previous Measurements of the Neutral Pion TFF in the space-like region

There are three sources of data for constraining the π^0 TFF in the low-Q^2 space-like region. Arguably the most important data point is the radiative width of the neutral pion, $\Gamma_{\pi^0\to\gamma\gamma}$, which fixes the normalization of $F_{\gamma^*\gamma^*\to\pi^0}(0,0)$. Results for the π^0 radiative width were recently published in *Science* [1]. Combining the PrimEx-I and PrimEx-II results gives

$$\Gamma_{\pi^0\to\gamma\gamma} = 7.802 \pm 0.052(stat) \pm 0.105(sys)\ eV$$

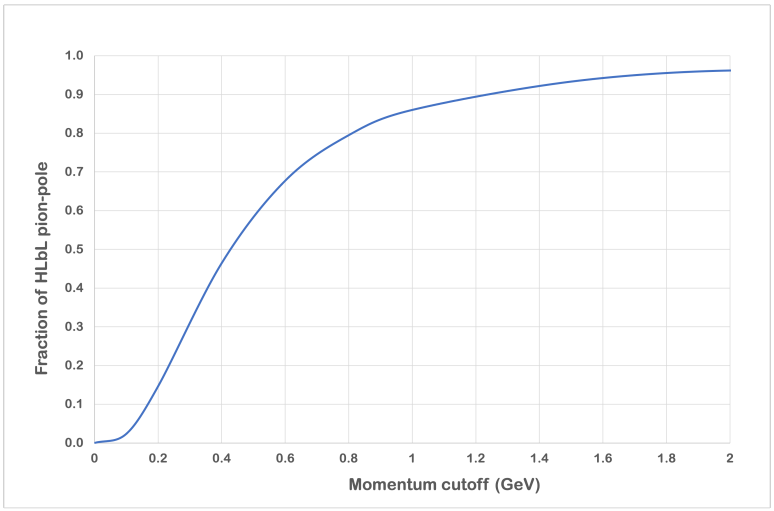

Figure 3: $a_\mu^{HLbL-\pi^0}$ as a fraction of the asymptotic limit as a function of the momentum cut-off in $Q_1 = Q_2$.

Experimental results for $\Gamma_{\pi^0\to\gamma\gamma}$ from PrimEx and previous measurements are shown in Fig. 4. The PrimEx result agrees with the Chiral Anomaly prediction, and deviates from NLO and NNLO corrections to the anomaly by two standard deviations.

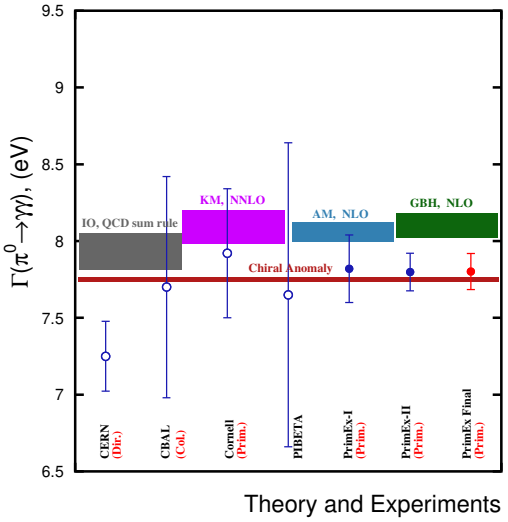

Figure 4: Measurements and calculations for the neutral pion radiative width.

The second source of data are from collider measurements, where $\gamma^*\gamma \rightarrow \pi^0$. The lowest Q^2 published measurements are by CELLO [4] and CLEO [5] in the Q^2 ranges 0.6 – 2.2 GeV^2 and 1.6 – 8.0 GeV^2, respectively. These measurements used the reaction $e^+e^- \rightarrow e^+e^-\pi^0$, where two photons are radiated by the colliding e^+e^- beams, one photon close to real and the second virtual, followed by $\gamma^*\gamma \rightarrow \pi^0$. Tagging either the e^+ or e^- allows for the determination of Q^2. There are also preliminary data from BESIII covering the range from 0.3 to 3.1 GeV^2 [3]. Radiative corrections for the BESIII data have not been finalized. Fig. 5 shows low-Q^2 data collected to date on the spacelike π^0 TFF.

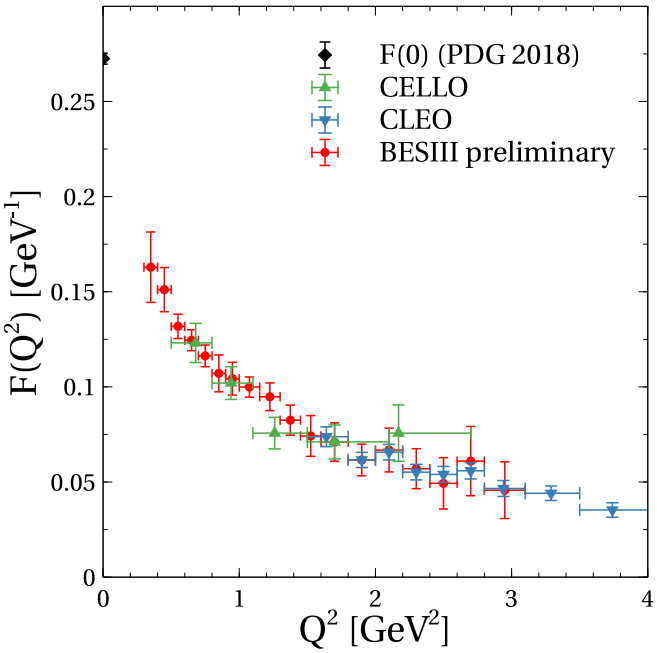

Figure 5: Momentum dependence of the space-like π^0 TFF for $Q^2 \leq 4\ GeV^2$. Data from CELLO[4] (green triangels (up)), CLEO[5] (blue triangles (down)), and preliminary data from BESIII[3] (red circles). Fig. taken from Ref. [13]

The third source of data are from the Dalitz decay $\pi^0 \rightarrow e^+e^-\gamma$. Although the Dalitz decay probes the time-like region of the TFF, the "slope" of the yield relative to e^+e^- invariant mass-squared is sensitive to the slope term a_π in Eqn. 1. In the low-Q^2 limit the Dalitz decay form factor is proportional to,

$$F(x) \propto 1 + a_\pi x$$

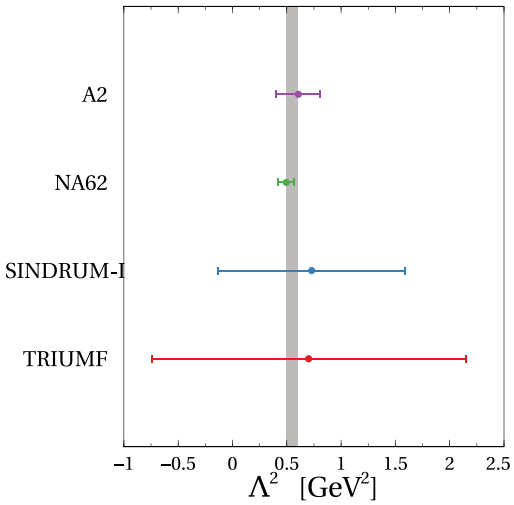

Figure 6: Slope parameter $\Lambda^2 = m_\pi^2/a_\pi$ of the timelike π TFF from Dalitz decays. The gray band shows the current average value and its uncertainty listed by the PDG. Fig. taken from Ref. [13]

where

$$x = \frac{m_{e^+e^-}^2}{m_\pi^2}$$

The most recent π^0 Dalitz decay measurements are from NA62 [6], an analysis of approximately 1.1M reconstructed Dalitz decays from $K^\pm \to \pi^0\pi^\pm$, and from the Mainz A2 collaboration [7], an analysis of approximately 0.5M reconstructed Dalitz decays from $\gamma p \to \pi^0 X$ @ $\Delta(1232)$. The A2 collaboration plans to continue data taking and expects to obtain an additional 2M reconstructed events. NA62 and A2 obtained $a_\pi = 0.0368(51)_{stat}(25)_{sys}$, and $a_\pi = 0.030(10)_{total}$ from their analyses, errors of approximately $\pm 15\%$ and $\pm 33\%$ respectively. A compilation of time-like slope parameter measurements is shown in Fig. 6, where the parameter $\Lambda^2 = m_\pi^2/a_\pi$ is plotted in the figure. The PDG average for a_π is 0.0335 ± 0.0031, an error of $\pm 9\%$. The PDG average is dominated by a fit to the CELLO data with a VMD form factor [4]. The combined statistical and systematic errors on CELLO fit for a_π is estimated at $\pm 11\%$.

Finally, we note that there is a significant data set on the *time-like* π^0 TFF measured in the reaction $e^+e^- \to \gamma^* \to \pi^0\gamma \to 3\gamma$ from CMD-2 [8] and SND [9, 10, 11]. However, a straight-forward technique to translate the TFF measured in the time-like region into the space-like region does not exist. Analytic continuation methods such as dispersion calculations must be utilized, hopefully without introducing a significant model dependence [13, 14].

In summary, FNAL E989 may soon reach the 5σ "gold standard" for discovery of physics beyond the Standard Model based on the disagreement of a_μ^{exp} with a_μ^{SM}. Given the importance of this possible discovery, we believe the existing experimental constraints on the low-Q^2 region of the π^0 TFF are unreliable. They are based on a limited low-Q^2 range that makes them inadequate for a precision measurement of $a_\mu^{HLbL-\pi^0}$, the largest single component of HLbL.

5 Experimental Setup

The proposed TFF measurement will use the PRad setup shown in Fig. 7, but with several critical improvements and modifications that include (i) the JLab fADC-125 readout system for the calorimeter, (ii) an additional GEM detector plane, and (iii) a solid target. The scattered electrons and π^0 decay photons will be detected simultaneously in HyCal, the calorimeter successfully used in the PrimEx-I, PrimEx-II, and PRad measurements

5.1 Beamline and detectors

Just as in the PRad experiment, the scattered electrons will travel through the 5 m long vacuum chamber with thin window to minimize multiple scattering and backgrounds. The vacuum chamber matches the geometrical acceptance of the calorimeter. The new GEM plane will be placed about 40 cm upstream of the GEM plane used in PRad, as shown in Fig. 8. The pair of GEM planes will ensure a high precision measurement of the GEM detector efficiency, and add a modest tracking capability to further reduce the beam-line background.

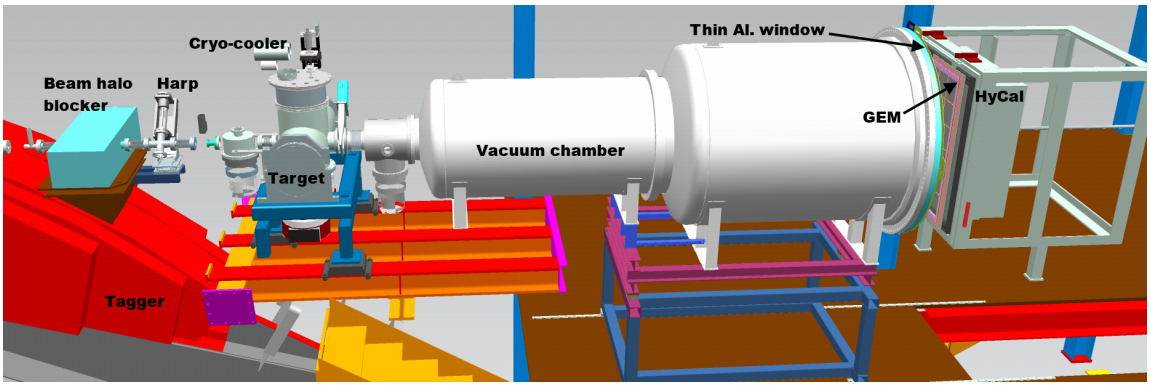

Figure 7: A schematic layout of the PRad experimental setup in Hall B at Jefferson Lab, with the electron beam incident from the left. The key beam line elements are shown along with the two-segment vacuum chamber, and the GEM and HYCAL detector systems.

The principle elements of the experimental apparatus along the beamline are as follows:

- Silicon target of thickness 250 μm
- Two stage, large area vacuum chamber with a single thin Al. window at the calorimeter end
- A pair of GEM detector planes separated by about 40 cm for coordinate measurement as well as tracking.
- HyCal calorimeter with high resolution $PbWO_4$ crystal calorimeter insert in the interior, and lead glass blocks on the exterior.
- The HyCal readout electronics should be converted from the FASTBUS based system used for PrimEx-I, PrimEx-II and PRad, to the standard JLab fADC-125 system.

The PRad collaboration has proposed upgrading the HyCal calorimeter to be an all $PbWO_4$ calorimeter, rather than the hybrid version. In this upgrade the lead-glass modules would be replaced with new $PbWO_4$ crystals, significantly improving the uniformity of the electron detection over the entire experimental acceptance. *While this upgrade is welcomed for the proposed TFF measurement, it is not essential. All of the simulations in this proposal assume the standard (non-upgraded) HyCal.*

We also note that the approved PRad-II experiment has requested funding for an upgrade to fADC-250 modules for HyCal readout. *While an upgrade to fADC-250s is beneficial to TFF, using fADC-125s does satisfy our experimental requirements.*

We note that the precision of the GEM detector efficiency contributed significantly to the systematic uncertainty of the PRad experiment. A high precision measurement of the GEM detector efficiency can be achieved by adding a second GEM detector plane. In this case, each GEM plane can be calibrated with respect to the other GEM plane instead of relying on the HyCal, minimizing the influence of the HyCal position resolution. It will also help reduce various backgrounds in the determination of the GEM efficiency, such as cosmic backgrounds and the high-energy photon background. In addition, the tracking capability afforded by the pair of separated GEM planes will allow measurements of the interaction point coordinate along beamline. This can be used to eliminate various beam-line backgrounds, such as those generated from the upstream beam halo blocker. The uncertainty due to the subtraction of the beam-line background, at forward angles, is one of the dominant uncertainties of PRad. Therefore, the addition of the second GEM detector plane will reduce the systematic uncertainty contributed by two dominant sources of uncertainties. PRad collaborators at UVa have committed to the construction of the second GEM plane for the approved PRad-II experiment.

Important upgrades are also in progress for the Hall-B beamline. The window on the Hall-B tagger will be replaced with an aluminum window, which is expected to result in a significant improvement in the beamline vacuum, particularly upstream of the target. This will help reduce one of the key sources of background observed during the PRad experiment. Further, a new beam halo blocker will be placed upstream of the Hall-B tagger magnet.

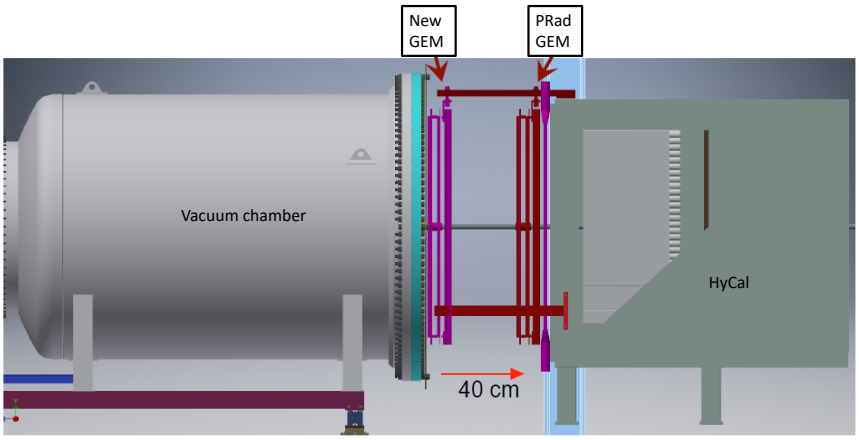

Figure 8: The placement of the new GEM chamber in the proposed experimental setup for PRad-II.

This will further reduce the beam-line background critical for access to the lowest angular range and hence the lowest Q^2 range in the experiment.

5.2 Silicon target

State-of-the-art Primakoff experiments as defined by PrimEx use a target with moderate atomic number (for a reasonable ratio of Primakoff to coherent production), ground state $J^\pi = 0^+$ (to simplify the reaction calculation), precisely determined nuclear charge distribution (for calculation of E.M. and strong form factors), and a target material and thickness choice that allows for ease of handling (for thickness studies and mounting). Silicon satisfies all of these criteria. Because of the success PrimEx-II had with data taking on silicon (see fig. 2), and the considerable effort that went into calculation of the coherent and incoherent backgrounds for silicon, we elected to utilize silicon as the target in the TFF measurement.

The target will be an approximately 250 μm thick silicon wafer, diameter from 1 to 2 inches, with natural isotopic abundance. This thickness is approximately 0.3 % radiation length. The amount of n-doping or p-doping in these crystals is effectively negligible for our purposes. To better understand multiple scattering effects in the data we will also take calibration data with a 100 μm thick silicon target mounted on the target ladder. Si wafers of this size and thickness are available from several manufacturers.

Electrons passing through crystal radiators produce coherent radiation (peaked at specific energies) and non-coherent radiation (with characteristic $1/k$ distribution). There are also channeling affects in electron transport. For this experiment it is preferable for the Si crystal to behave as an amorphous target. The simplest way to do this is to not align the

principle symmetry axis of the Si crystal, the (1,0,0) crystal orientation, with the beamline. We can also consider using a Si wafer with (1,1,1) orientation, or a Si wafer with (1,0,0) orientation and rotate the normal vector to the disk around the beam-line x and y axes by $\sim 45^\circ$.

Silviu Dusa at JLab has performed an assessment of target beam heating using the computational fluid dynamics (CFD) code ANSYS-FLUENT. Fig. 9 shows the calculated equilibrium target temperature across the central axis of the target assuming a 25 mm diameter, 25 μm thick Si target, and an unrastered 0.55 μA, 100 μm diameter electron beam. The figure indicates a modest central temperature rise of $\sim 2^\circ$ K. For the proposed running conditions of TFF, 250 μm thick Si and 10 nA beam, beam heating is reduced by a factor of ~ 0.2 relative to the CFD calculation shown here, and heat transport from the beam spot increased by a factor of ~ 10 (due to increased target thickness). *Therefore, we conclude that target beam heating is not a limiting factor in setting the luminosity of the measurement.*

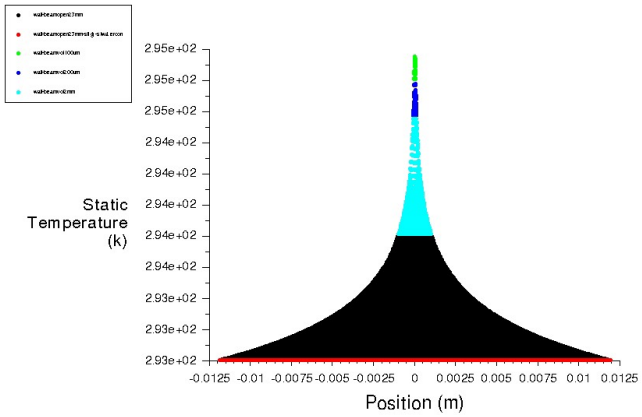

Figure 9: Beam heating of a 25 mm diameter, 25 μm thick Si target for a 0.55 μA, 100 μm diameter, unrastered electron beam.

5.3 DAQ trigger

The TFF experiment requires that the original HyCal FASTBUS readout electronics be replaced with borrowed or new JLab fADC-125 modules. A total of 1,728 channels of fADC-125 are required to instrument the 1,152 channels of $PbWO_4$ crystal, and 576 channels of lead-glass blocks. We are in discussions with the Hall B DAQ group as to the best path forward to realize this requirement.

The DAQ trigger for the proposed TFF experiment will be organized from fADC-125 energy measurements in each block of HyCal. The trigger schemes under study require two or three clusters of energy in HyCal, each cluster with energy greater than 0.3 or 0.4 GeV, and a total energy sum of 4 GeV or greater. This type of trigger will be able to effectively select the expected three electromagnetic particles in the final stage of the reaction (the scattered electron and two decay photons from the forward produced neutral pion). The only significant contamination will be from time-accidental events from either deep inelastic scattering eA, and/or e^-e^--Møller production, both of which are high cross section processes. However, the good timing resolution of HyCal equipped with the FADC electronics (~ 2 ns) will make these out-of-time backgrounds a small part of the total DAQ trigger rate.

Estimated trigger rates are presented in section 7.

6 Acceptances and resolutions

The proposed experimental setup is sensitive to elecron scattering angles θ_e larger than $\sim 0.6^\circ$. In this section we present our results for the Primakoff cross section (see Eqn. 3) calculated using the technique described in Ref. [29]), and with acceptance related to the $\theta_e > 0.5^\circ$ limitation.

Figure 10 shows the Primakoff differential cross section as a function of the scattered electron energy for Q^2 ranges $0-0.3\,\mathrm{GeV}^2$ and $0-1.0\,\mathrm{GeV}^2$, and constant π^0 transition form factor ($F_{\gamma^*\gamma^*\to\pi^0} \equiv 1$). The corresponding integrated cross section values are 2.31 nb and 2.36 nb.

Geometric acceptance and reconstruction efficiency for Primakoff production have been estimated with the GEANT Monte-Carlo package. Simulated events were reconstructed using a program similar to that used for the HyCal calorimeter in the PrimEx-II experiment. The selection criteria for reconstructed events to be accepted were: (i) minimum energy of 0.5 GeV for a particle in the calorimeter (this is the same threshold PrimEx-II used for HyCal reconstruction); (ii) maximum energy of 4.5 GeV for the scattered electron, as acceptance drops sharply at this energy (see Fig. 11); (iii) the reconstructed π^0s should have an invariant mass within ± 10 MeV of 135 MeV (this is approximately 3 detector standard deviations); (iv) energy conservation in the detected event within ± 0.5 GeV; (v) γ's from π^0 decay should not overlap with charged particles in the GEM detector within 2 cm in both the X- and Y-directions. The charged particles can originate from the same event, or be accidental beam electrons within the 40 ns time acceptance window. Obtained efficiencies as a function of Mandelstam t and Q^2 for the Primakoff π^0 electro-production are shown in Figs. 12 and 13. The plots show that the efficiency is very significant, 30% or higher, for the main region of interest, $0.01\,GeV^2 < Q^2 < 0.3\,GeV^2$.

The π^0 invariant mass resolution, $\sigma \sim 3.3$ MeV, and total event energy resolution, $\sigma \sim 150$ MeV, are shown in Figs. 14, and 15. The mass resolution is worse than the 2.4 MeV

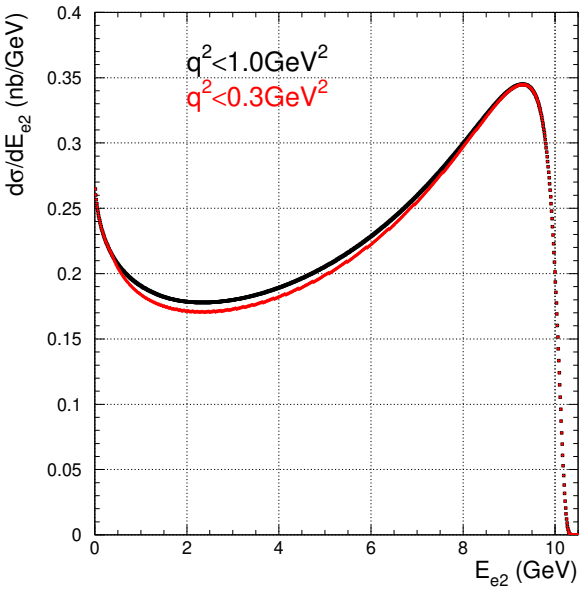

Figure 10: Primakoff differential cross section integrated over solid angles as a function of the scattered electron energy for Q^2 in the range $0-0.3$ GeV^2 (red dots), and $0-1.0$ GeV^2 (black dots) ranges. In this plot the incident electron energy is $E_0 = 10.5$ GeV, and the π^0 TFF is taken to be constant, $F_{\gamma^*\gamma^*\to\pi^0} \equiv 1$

value obtained in the PrimEx-II analysis because we are using the entire hybrid calorimeter, including the lead glass part, whereas PrimEx-II used just the lead-tungstate crystal insert. The relative Q^2 resolution as a function of Q^2, $\sim 3\,\%$, is shown in Fig. 16. Mandelstam t resolution divided by $\sqrt{t}$ is shown in Fig. 17. Figs. 18 and 19 show the resolution in θ_π, the angle between the virtual photon beam momentum $\vec{q}$ direction and the neutral pion momentum $\vec{k}_\pi$ direction. This resolution is in the $0.02^\circ - 0.03^\circ$ range, close to the resolution obtained in PrimEx-II. Resolutions of this order are more than adequate to resolve the Primakoff peak from the coherent background (see Fig. 2). The electron scattering angle resolution will depend on the target thickness. Fig. 20 shows the scattering angle resolution for a 250 μm thick silicon target as a function of the scattered electron energy. The resolution roughly follows a $\frac{0.024^\circ}{(E_e[GeV])^{0.85}}$ dependence, shown by the dashed line in the figure.

Fig. 21 shows the Primakoff differential cross section integrated over scattered electron solid angle and energy (within 0.5–4.5 GeV range) as a function of the π^0 production angle. The corresponding simulated π^0 yield scaled to the proposed 60 days of running is shown in Fig. 22; the plot doesn't include the projected yield from nuclear coherent production. There is a shift in the maximum of the Primakoff distribution from 0.02° to 0.04° due to

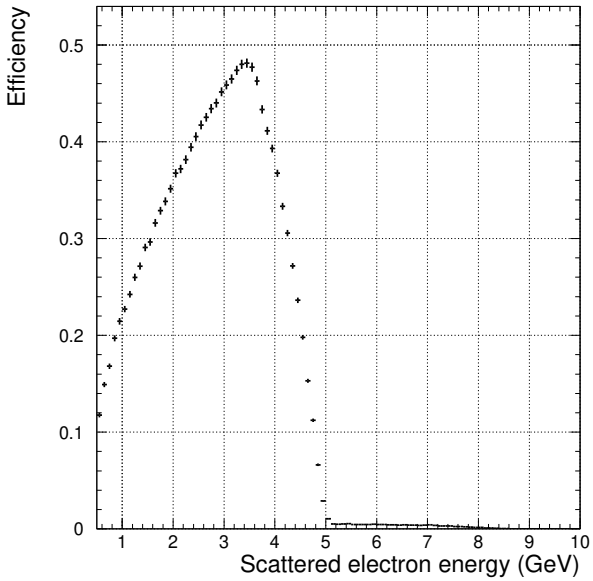

Figure 11: Detection efficiency vs scattered electron energy at an incident electron energy of $E_0 = 10.5\,\mathrm{GeV}$

resolution.

We conclude that the proposed experiment entirely complements the BESIII and CELLO measurements in covering the low Q^2 region with good acceptance and resolution.

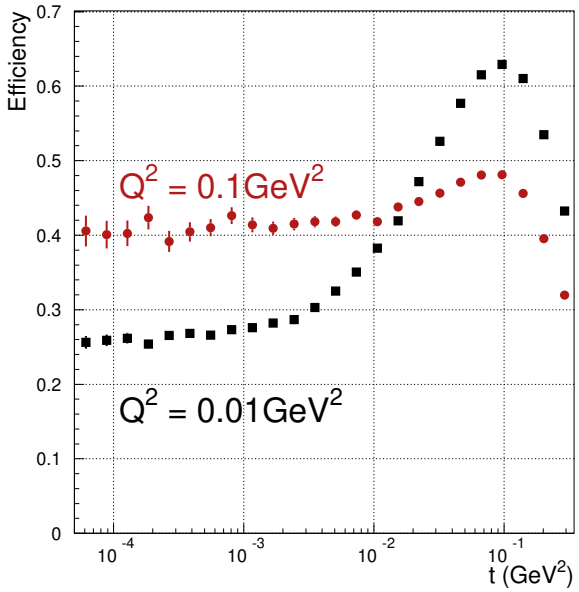

Figure 12: Detection efficiency vs Mandelstam t for $E_0 = 10.5$ GeV, scattered electron energy range 0.5...4.5 GeV, and $Q^2 = 0.01$ GeV^2/c^2 (black squares), and $Q^2 = 0.1$ GeV^2/c^2 (red dots).

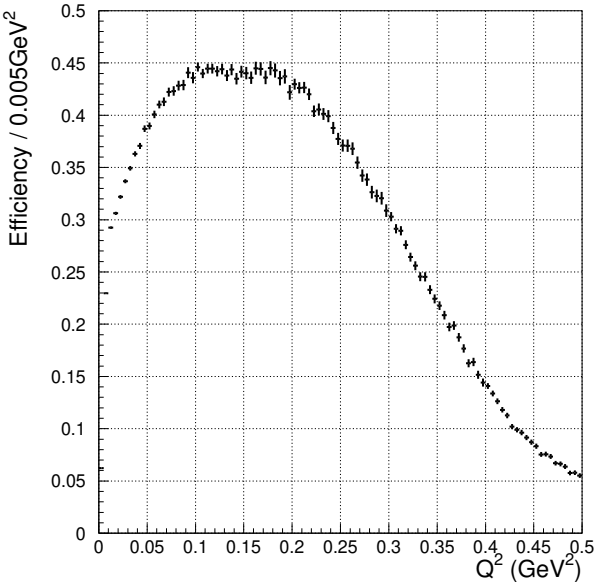

Figure 13: Detection efficiency integrated over Mandelstam t vs Q^2 for $E_0 = 10.5$ GeV, and scattered electron energy range 0.5...4.5 GeV

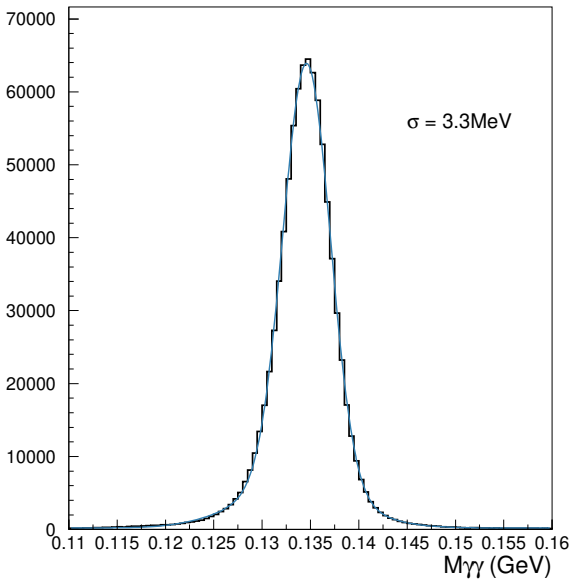

Figure 14: π^0 invariant mass resolution

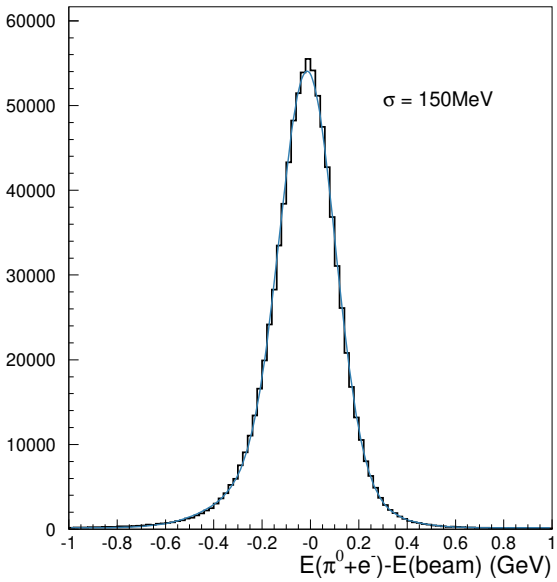

Figure 15: Event total energy resolution

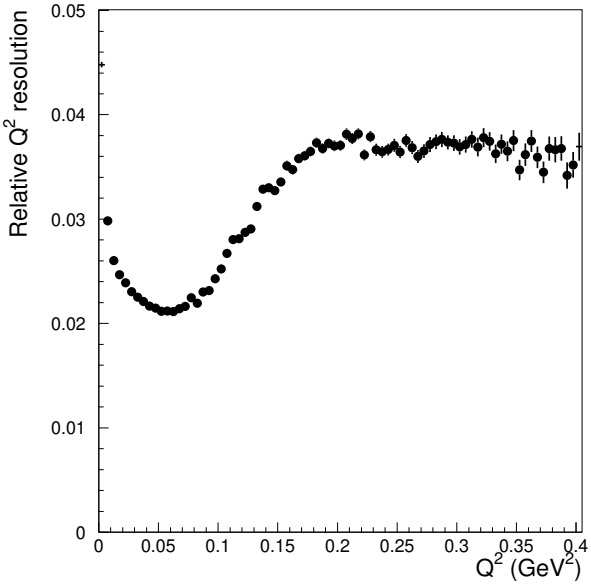

Figure 16: Relative Q^2 resolution vs Q^2, $E_0 = 10.5\,\mathrm{GeV}$

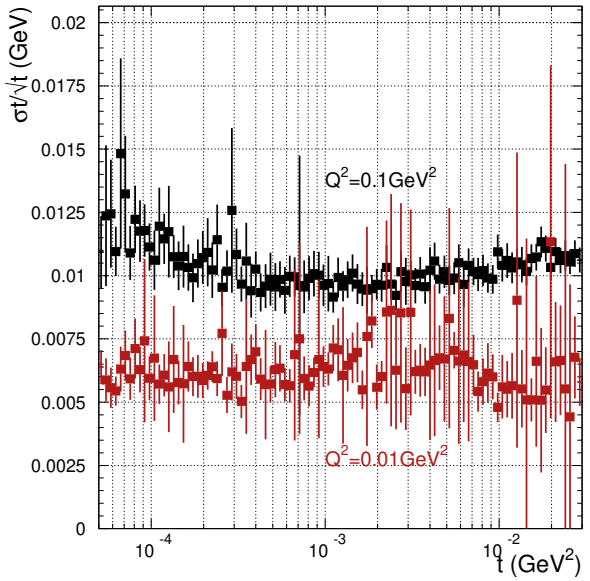

Figure 17: t resolution over $\sqrt{t}$ as a function of t for $Q^2 = 0.01$ (red points), and $0.1\,\mathrm{GeV}^2$ (black points), $E_0 = 10.5\,\mathrm{GeV}$

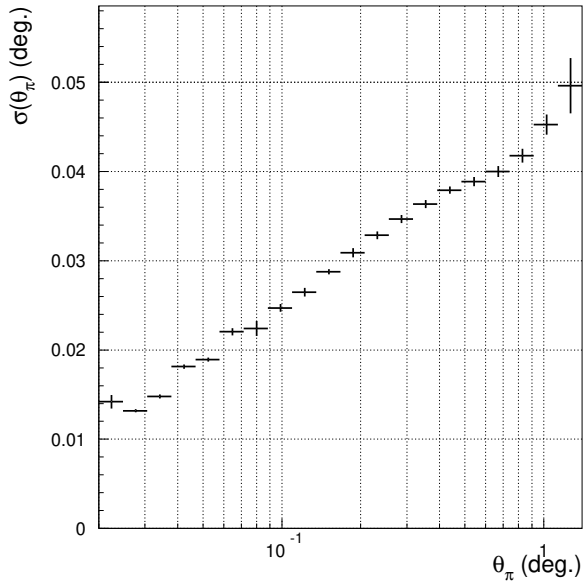

Figure 18: Resolution in θ_π vs θ_π, at $E_0 = 10.5$ GeV. θ_π is the angle between the virtual photon beam momentum $\vec{q}$ and the neutral pion momentum $\vec{k}_\pi$.

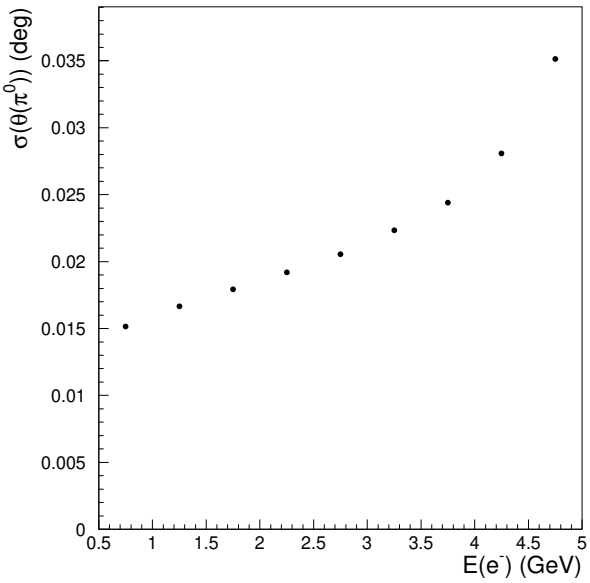

Figure 19: Resolution in θ_π vs scattered electron energy, at $E_0 = 10.5$ GeV

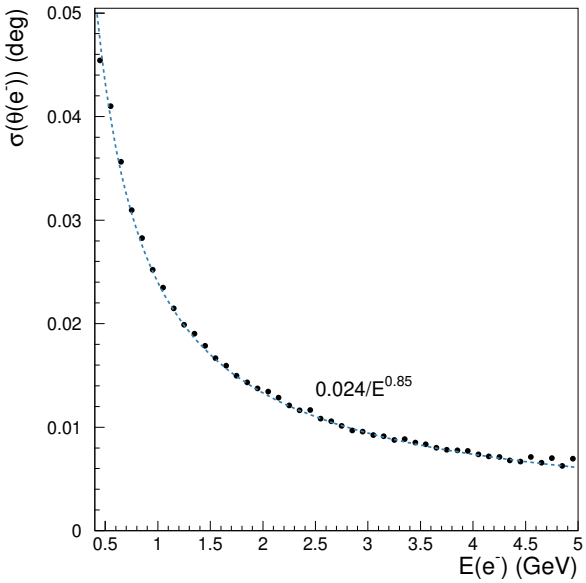

Figure 20: Resolution in the electron scattering angle vs scattered electron energy, at $E_0 = 10.5$ GeV. The dashed line shows the $\frac{0.024^\circ}{(E_e[GeV])^{0.85}}$ fit.

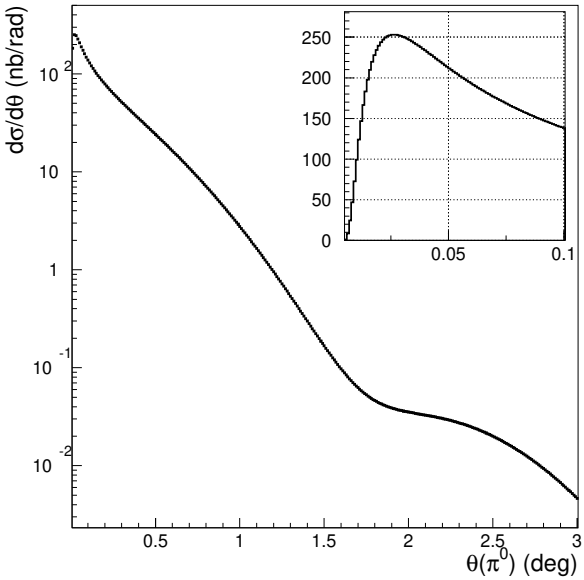

Figure 21: Primakoff differential cross section integrated over scattered electron solid angle and energy (within 0.5–4.5 GeV range) as a function of π^0 production angle

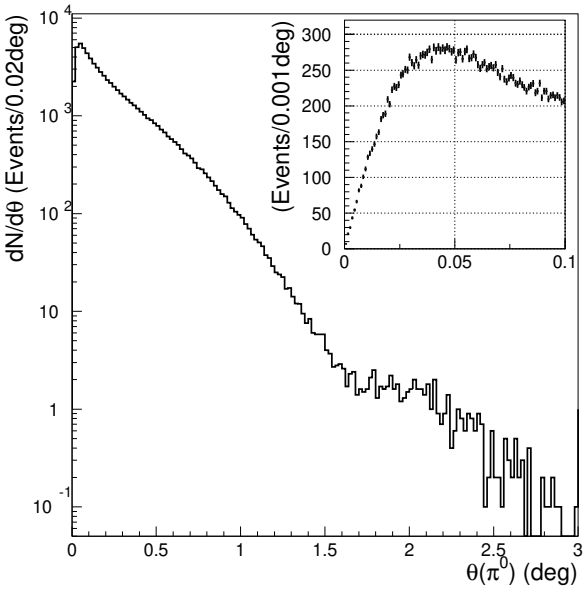

Figure 22: Simulated π^0 yield scaled to the proposed 60 days of running statistics as a function of π^0 production angle. Yields from coherent production are not included.

Table 1: PRad runs used for cross-checking trigger rates and their parameters

PRad run number	target	Beam current [nA]	Beam energy, [GeV]	trigger threshold, [GeV]	prescale factor	DAQ live-time	Trigger rate [kHz]
1495	H gas	55	2.15	0.7	0	89%	3.97
1501	carbon	1	2.15	0.7	2	91%	8.86
1515	empty	55	2.15	0.7	0	98%	0.67

7 Trigger rates and radiation dose

To estimate trigger rate and radiation dose in the calorimeter we have performed simulations of electromagnetic processes in the target and their effect on HyCal response using GEANT program package.

The main contributions to the background rate are from (i) delta electron production, and (ii) multiple scattering in the target, the latter causing the incident beam to interact occasionally with the inner layers of the calorimeter. Bremsstrahlung production also contributes to the background, with a rate smaller than the other two backgrounds. Rates have been estimated based on the luminosity proposed to PAC 48 in our letter of intent: 25 μm silicon target and 100 nA electron beam current. Since the multiple scattering effect grows slower than linear with increasing target thickness, we tested several combinations of target thickness and beam current while keeping the product of the two constant to see how best to optimize the experiment. The main limiting factor for the product is the channel rate in the inner-most part of HyCal, caused primarily by the scattered incident electron beam. To keep this contribution at an acceptable level, we plan to increase the thickness of the tungsten absorber installed in front of the central HyCal crystals from 6 to 15 cm, and expand the transverse size of the absorber from 4×4 to 6×6 HyCal modules. Fig. 23 shows calorimeter module rates for the most background loaded layers as a function of target thickness and beam current, with the product being held fixed. Even with the increased absorber thickness the rate in the most inner layer of HyCal is still too high – more than 2 MHz for the thinnest target, and caused primarily by the scattered incident beam hitting the central crystals. Therefore, we propose to turn off HV for this layer. The rate in the second inner layer protected by the enlarged absorber is acceptable, within 250 kHz.

To cross-check our trigger rate calculations we have changed geometry setup (target, tungsten absorber) to the PRad experiment and compared the obtained values with the observed during PRad run. We have selected three PRad runs with hydrogen gas, empty, and carbon targets installed (table 1).

The simulation results show reasonable agreement with the observed rates. Table 2 shows

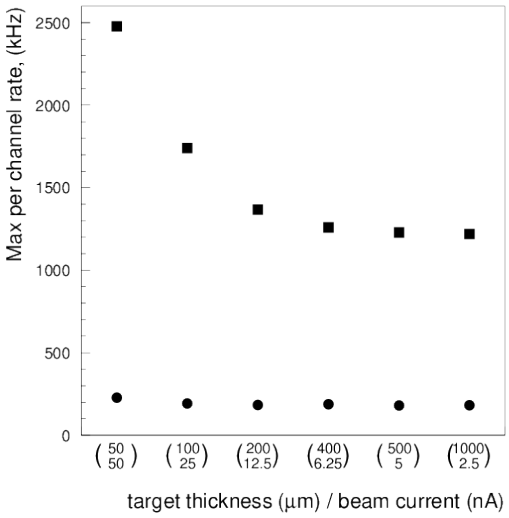

Figure 23: Estimated HyCal module rates. Squares – most inner HyCal layer around the beamline, circles – the second inner layer.

Table 2: Comparison of PRad trigger rates with Monte-Carlo simulation

Target	Beam current [nA]	Beam energy, [GeV]	trigger threshold, [GeV]	Observed trigger rate [kHz]	Simulated trigger rate [kHz]
H_2 gas, $1.875\times10^{18}\ \frac{atoms}{cm^2}$	55	2.15	0.7	3.8	2.8
carbon, $1\,\mu m$	1	2.15	0.7	29.2	12

this comparison, the measured rates were normalized to 100 % DAQ livetime, no trigger prescale factor, and empty target rate subtracted. The discrepancy with the carbon target could be caused by its very small thickness and the large uncertainty on the small thickness.

We also note, that single Møller scattering was responsible for the main part of trigger events in PRad, but for the proposed experiment it can not open trigger due to its kinematics and higher trigger threshold, and beam multiple scattering for large angles gives the main contribution.

The Møller scattering remains the dominant process at 10.5 GeV electron beam energy deserving a more detailed glance. Fig. 24 shows the geometry of the symmetric Møller pair which hits the tungsten absorber at the minimum distance to its edge of 0.7 cm never reaching open HyCal modules. Thus only "single arm" Møller events can hit HyCal.

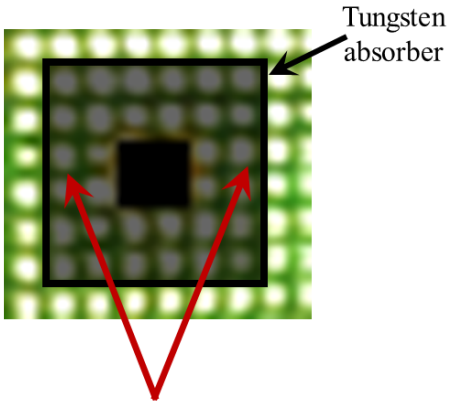

Figure 24: Schematic view of the symmetric Møller event: electrons with equal energies (shown with red arrows) hit the central part of the calorimeter protected by the absorber (dark square). Electron tracks are entirely within the absorber area.

Table 3: Topology of Møller events hitting the calorimeter area and their rates for the different zones shown on the scheme below

Zone	Møller angle in the CM frame [rad]	Møller angle in the lab frame [deg]	Calorimeter hit to beam-line distance [cm]	Electron energy range [GeV]	Integrated Møller rate [kHz]	Maximum Møller event per module rate [kHz]
1*	1.47–1.93	0.49–0.79	5–8	5.77–3.33	15	1.2
2	1.93–2.5	0.79–1.7	8–17.2	3.33–1.05	190	1.5
3	2.5–2.8	1.7–3.25	17.2–33	1.05–0.3	630	1.3
4	2.8–2.95	3.25–5.9	33–60	0.3–0.095	1940	3.5
5	2.95–3.00	5.9–8.2	60–84	0.095–0.045	400	2.2

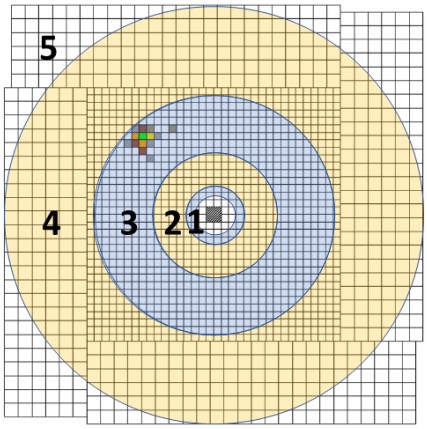

Table 3 shows Møller rates integrated over HyCal acceptance obtained from the simulation for the different calorimeter zones (shown on the scheme below the table) together with the Møller event per module rates, particle production angles, energy, and distance of track intersection with HyCal face to the beam axis. The rate values perfectly match simple analytical calculations. The energy of electrons hitting HyCal for such events remains below the threshold of 4 GeV excluding very small area (inner part of zone 1 on the scheme), where it can reach 4.7 GeV. The number of counters and integrated rate are increasing from inner to outer zones, and hit energy decreasing the same time, while per module rates remain at few kHz level. Hit energy distribution and 2-D plot for hit to beam axis distance vs energy shown on fig. 25. Møller events marked with red color. As seen from the energy distribution histogram, the most of events above the trigger threshold are elastic beam scattering on atomic nuclei with very small addition from Møller events.

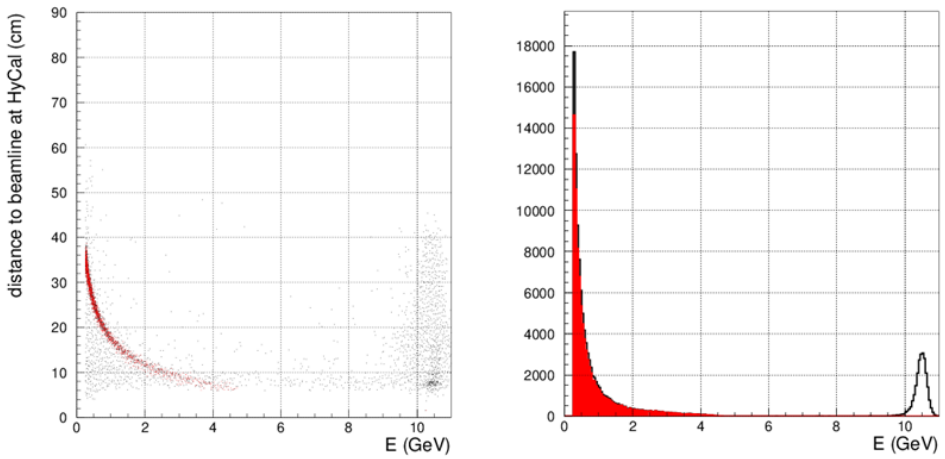

Figure 25: Calorimeter hit distribution on energy (right plot) and distance to beam axis vs energy (left plot). Black histograms – all hits, red – Møller events.

Fig. 26 shows the radiation dose rate for layers in HyCal. The radiation dose is highest in the shielded inner-most layer, where it ranges from 8 to 11 rad/hr when excluding the 50 μ target/50 nA beam-current combination. The dose is 4 to 6 rad/hr for the unshielded third and fourth layers. According to studies [30, 31] this may result in a 2%–5% light yield degradation in the module due to the radiation effects.

Fig. 27 shows the calorimeter trigger rate for a simple 4 GeV total energy threshold for several combinations of target thickness and beam current, at fixed luminosity. The trigger rate is estimated to be approximately 250 kHz, which is unworkable for the experiment. For that reason we require the implementation of the more sophisticated trigger scheme described in section 5.3.

Fig. 28 shows the estimated trigger rate when two or three clusters are required in the calorimeter, each cluster with energy greater than 0.3 or 0.4 GeV, and a total energy sum of 4 GeV or greater. Clusters are defined as simple 3×3 module areas in HyCal which may not intersect with each other. In this case the trigger rate reduces to 25 kHz at the highest and 4 kHz at the lowest, which can be handled by the Hall-B DAQ system. Such trigger logic can be organized and requires upgrading the calorimeter readout electronics with fADC-125 modules [32].

Using HyCal energy deposition in the trigger requires a gain equalization procedure to avoid systematics related to the trigger inefficiency. This will be done by placing HyCal

*The most part of zone 1 is covered by the absorber

on the transporter and scanning in the low intensity photon beam produced in the photon tagger with the electron beam energy reduced to about 5 GeV. This procedure has been performed previously during the PrimEx and PRad experiments and takes about 3 days of beam time and 3 days for placing HyCal on the transporter and back.

In summary, we propose to switch off HV for the inner-most layer in HyCal, increase the tungsten absorber transverse size by factor of 1.5, and thickness by 2.5. The trigger should be configured to require two or three clusters of energy in the calorimeter, each with energy greater than 0.3 or 0.4 GeV, and with a total energy sum requirement of 4 GeV. Running with a 250 μm Si target and 10 nA beam current gives an estimated trigger rate in the 3.5 to 20 kHz range. The estimated DAQ trigger rates and radiation dose to the HyCal modules are estimated to be acceptable for running the experiment.

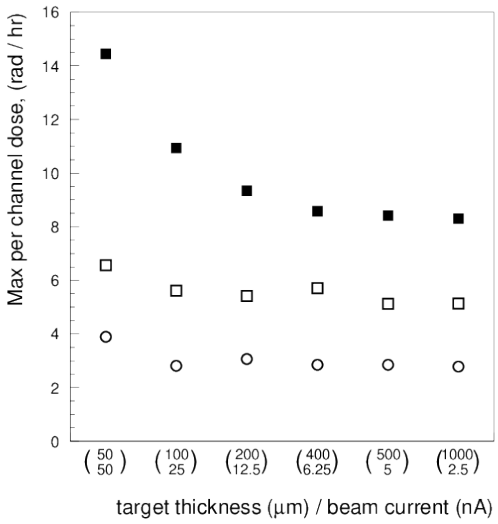

Figure 26: Estimated radiation dose rate per hour. Solid squares – most inner HyCal layer around the beamline, open squares – the third inner layer (first unshielded layer), open circles – area outside the third inner layer.

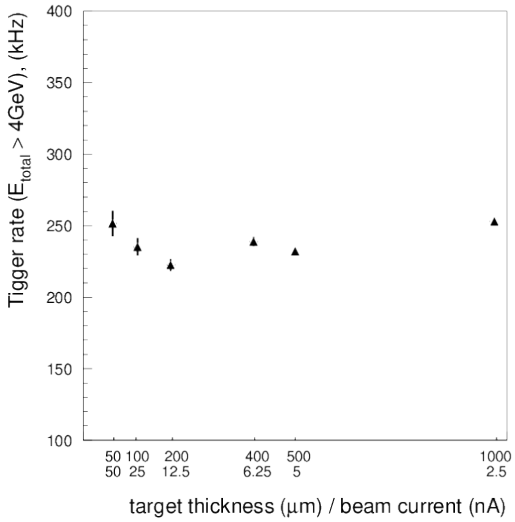

Figure 27: Estimated HyCal trigger rates for the simple total energy sum trigger with the threshold of 4 GeV

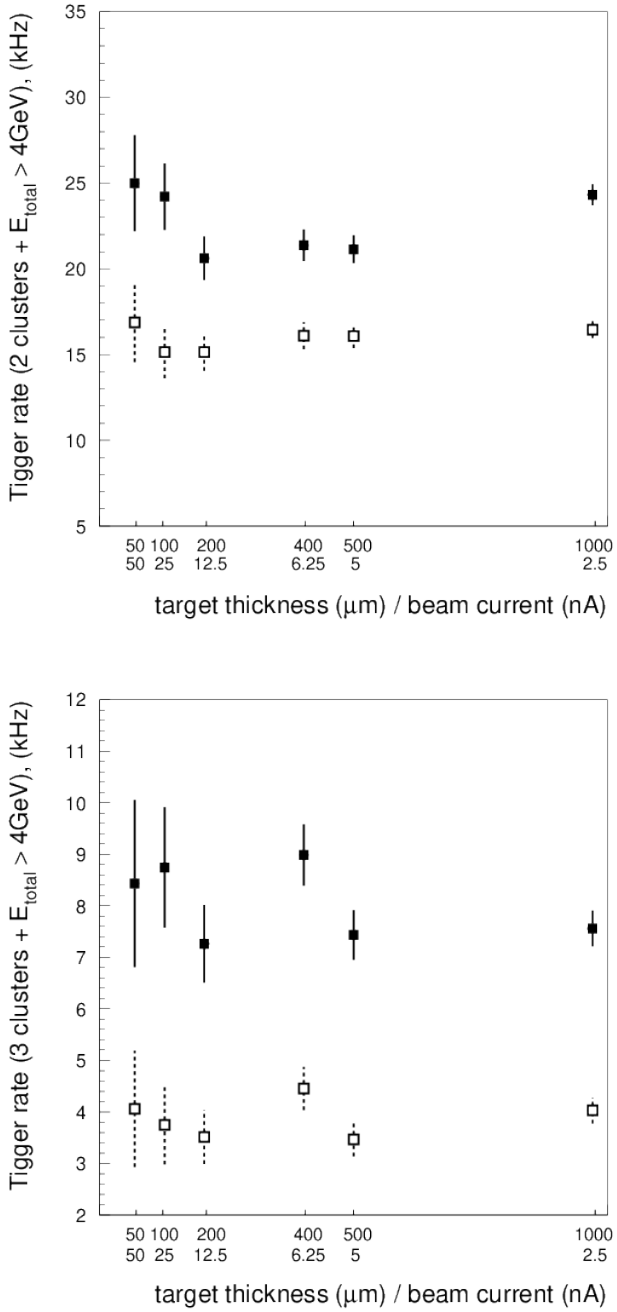

Figure 28: Estimated trigger rates for events with total energy deposition in HyCal more than 4 GeV and at least two clusters (top), or three clusters (bottom) found. The minimum cluster energy is 0.3 GeV (solid squares), or 0.4 GeV (open squares).

8 Data Rates and beam time

8.1 Signal yield

To estimate the integral event rate for the Primakoff events we ran MC simulations with the following fixed parameters and intervals:

- Target: 250 μm silicon
- Beam energy: 10.5 GeV
- Beam current: 10 nA
- Angular range of the scattered electrons: $> 0.5^\circ$
- Energy range of the scattered electrons: $0.5 \div 4.5$ GeV
- Full range of expected Q^2 values up to 1 GeV^2
- γs from neutral pion decays should have energy at least 0.5 GeV, and not overlapped with any charged particle in the GEM detectors

The total Primakoff cross section integrated over the scattered electron energy range of 0.5...4.5 GeV is estimated to be $\Delta\sigma = 0.65 \cdot 10^{-3}$ μb. With these numbers and simulated geometrical acceptance, the Primakoff event rate in the proposed experiment is $\approx$1000 events/day or $\approx$60,000 events/60 days. Therefore, for an estimated 60 days of beam time we will be able to accumulate approximately 60 K useful events over the Q^2 range from .003 to 0.3 GeV^2.

8.2 Signal-to-background in two-photon invariant mass distributions

There are two main contributions to the background: electromagnetic and hadronic.

To estimate the backgrounds from electromagnetic processes extensive studies have been performed: 6×10^{15} events of the electron beam interacting with the 250 μm thick silicon target have been simulated. This corresponds to about 26.5 hours of 10 nA beam current. Events were sampled by 40 ns bunches with 2,500 events per bunch. Bunches with at least 7.5 GeV total energy deposition in the calorimeter and 3 particles each with a minimum energy of 50 MeV going into the calorimeter acceptance (including the absorber area) have been recorded for further processing. The selected events have been propagated through the experimental setup and reconstructed. During reconstruction we assumed that charged particles (mostly electrons) can be misidentified as neutrals with 1% probability, which is a reasonable estimation based on our previous experience with the PRad GEM. In the reconstructed event we selected particles with energy greater than 0.5 GeV, and required that there should be at least two neutral particles for π^0 reconstruction and a third one

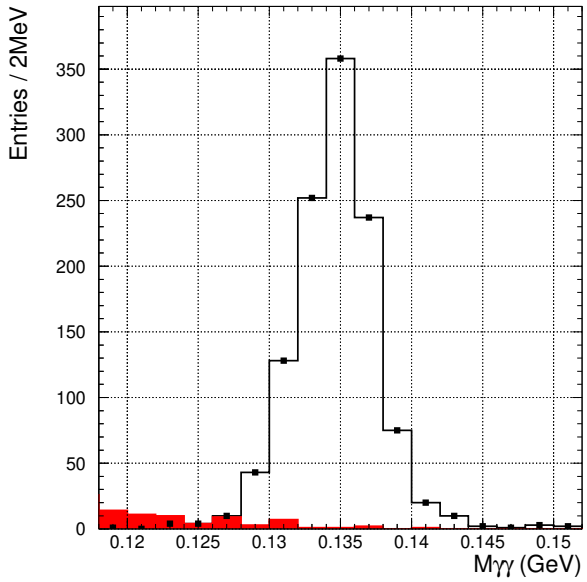

Figure 29: Invariant mass of two neutral clusters in the calorimeter. Expected statistics for one day of running. Open histogram – Primakoff π^0, red solid histogram – electromagnetic background

(mimicking the scattered electron) with the total energy of triplet within a $\pm\,1$ GeV window around the beam energy. The result of this background simulation for the invariant mass of the false π^0 candidates is shown in Fig. 29. We put the expected events from Primakoff production for the same running time, one day of running, on the same plot for comparison. We note that the calorimeter timing resolution obtained during the PrimEx experiment was better than 2 ns, which should suppress most of the background obtained with the $\pm$20 ns timing window shown in Fig. 29. The dependence of the number of background events as a function of the coincidence time window is shown in Fig. 30.

The main hadronic backgrounds are from π^0 and ω meson (with "forward" $\omega \rightarrow \pi^0\gamma$ decay) photo-production with the incident real photon produced by bremsstrahlung in the target. To pass the analysis selection criteria these processes must have a complementary electron that satisfies the energy conservation condition. The electron in the event could be either an incident beam electron rescattered in the target, or any background electron that's accidentally in time and satisfies energy conservation with the π^0, i.e. within $3\,\sigma$ of the apparatus energy resolution. The virtual photon beam angle in the lab frame has values in the range from 0 up to $\sim 1^\circ$. The direct π^0 photoproduction cross section is well studied [1] and has cross section of $\sim 1.5\,\mu$b (at 5 GeV photon beam energy) if integrated from 0 to 2.4 $^\circ$ angle of the pion. With the proposed experimental setup we estimate the

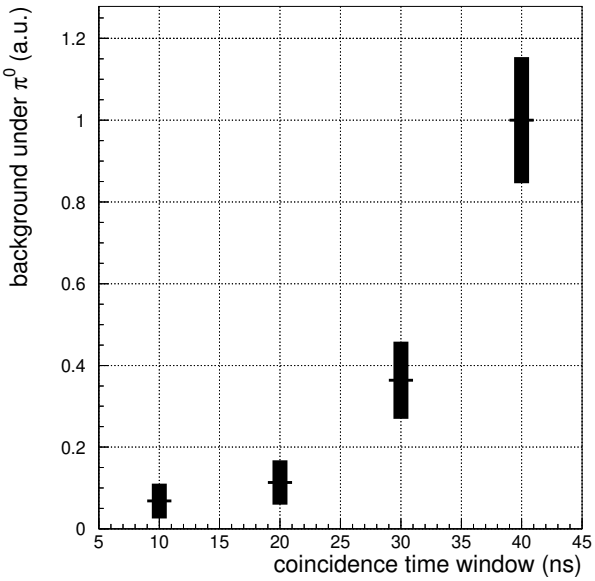

Figure 30: Dependence of the number of electromagnetic background events underneath π^0 mass peak as a function of the coincidence time window size

background yield contribution from this process to our data within 50 events for the entire run. ω meson photoproduction cross sections have values of $\sim 30\ \mu$b (coherent mechanism), and $\sim 70\,\mu$b for the incoherent contribution [33, 34]. Even this source has a significantly higher cross section, it is suppressed by $\omega \to \pi^0\gamma$ decay branching and, in addition, the scattered electron can not satisfy the energy conservation (only accidental scattered beam electrons can be coupled with such pions to pass through analysis criteria). Our estimation for this background yield contribution is below 350 events for the 60 days of running. Thus we expect the total hadronic background contribution to be within a percent level. This contribution will be subtracted using well-known production parameters affect the measurement systematics well below percent level.

9 Cross section normalization

In addition to the direct electron beam flux measurement, which we expect to have an uncertainty at sub-percent level, we will use Moller scattering for the additional normalization. This process is well studied and can easily be measured with very high statistics. It has a very distinct signature: relationship between scattered electron energy and angle. The setup provides the excellent acceptance for such measurement by detecting one of two scattered electrons. Fig. 31 shows relationship between scattering angle and energy for the

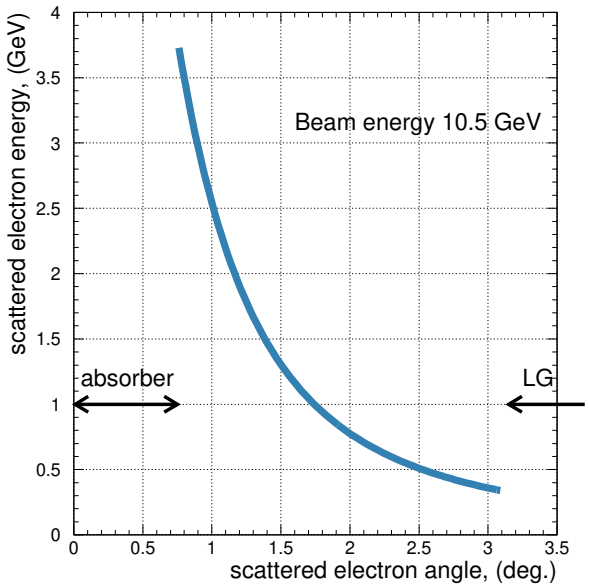

Figure 31: 2-dimensional distribution of Moller scattering electrons energy and angle. Arrows show regions corresponding to absorber and lead glass part of the calorimeter.

outgoing electrons. We will setup an additional total energy deposition in the calorimeter trigger to record such events with the threshold of $\sim$1 GeV for the inner part (12x12 modules) and ~ 0.2 GeV for the outer part, which will be prescaled by 3 orders of magnitude. The exact energy thresholds and scale factors will be briefly optimized during commissioning run after the gain equalization procedure. The Moller cross section measurement will have the same level of the systematic error budget components value (setup acceptance, calorimeter energy response, target properties) as we observed during the neutral pion photoproduction cross section measurement [1] (0.7...0.8%). In conjunction with the direct beam flux measurement we expect to have the luminosity uncertainty control at the sub percent level.

The radiative effects that have been applied in the simulation and the radiative corrections (RadCor) that must be applied to the data are discussed in Appendix C. Here we note that the necessary QED techniques are straight forward, and that S. Srednyak, who worked on RadCor for PRad, has agreed to work on this aspect of the data analysis for TFF.

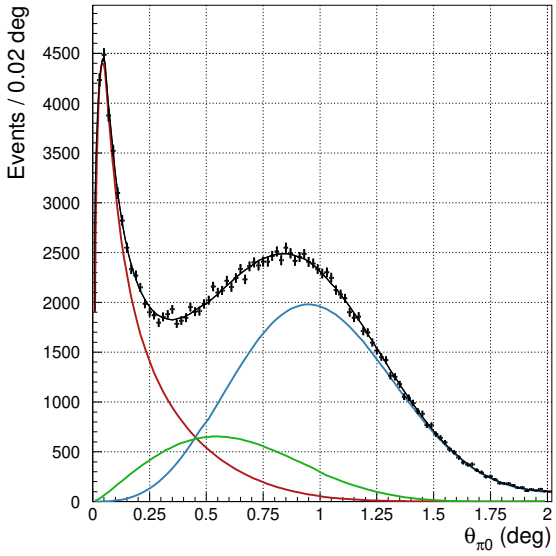

Figure 32: Simulated detected yield for π^0 electroproduction. Curves show input from Coulomb (red), strong coherent (blue), and their interference (green) production mechanisms.

10 Results from fitting pseudo-data: projected sensitivities to the TFF, HLbL, and target choice

To estimate this experiment sensitivity to the TFF parameters (Eq. 1), we have simulated data samples with Coulomb (Eq. 3), strong coherent (Eq. 16) production mechanisms and their interference. We have taken for the simulations the interference phase value of 1 rad observed in photoproduction on silicon [1]. The expected yield for the proposed luminosity shown in Fig. 32 (for the entire Q^2-range) and in Fig. 33 (for the selected 0.01 GeV^2-wide Q^2-bins), production mechanisms contributions shown in color curves. To extract TFF parameters, the simulated data were split in 30 bins of Q^2: from 0 to 0.3 GeV^2, then the Coulomb yield was normalized to the expected yield from the simulation with TFF set to 1.

In our analysis we fit the distribution for square root of the resulting ratio (fig.34) with the simple equation: $\sqrt{Yield\ ratio} = Constant - Slope \cdot Q^2 + Quadrature\ term \cdot Q^4$. For the expected statistics we are able to extract slope and quadrature parameters (corresponding to a_π and b_π in eq. 1) with the relative uncertainties of 6 % and 17 %, and the constant term with an uncertainty of 0.35%. The estimated uncertainty in the constant term corresponds to a 0.7% stat. error in the $\pi^0 \to \gamma\gamma$ decay width, and the estimated uncertainty in the slope term corresponds to a 3% error in the neutral pion electromagnetic transition radius.

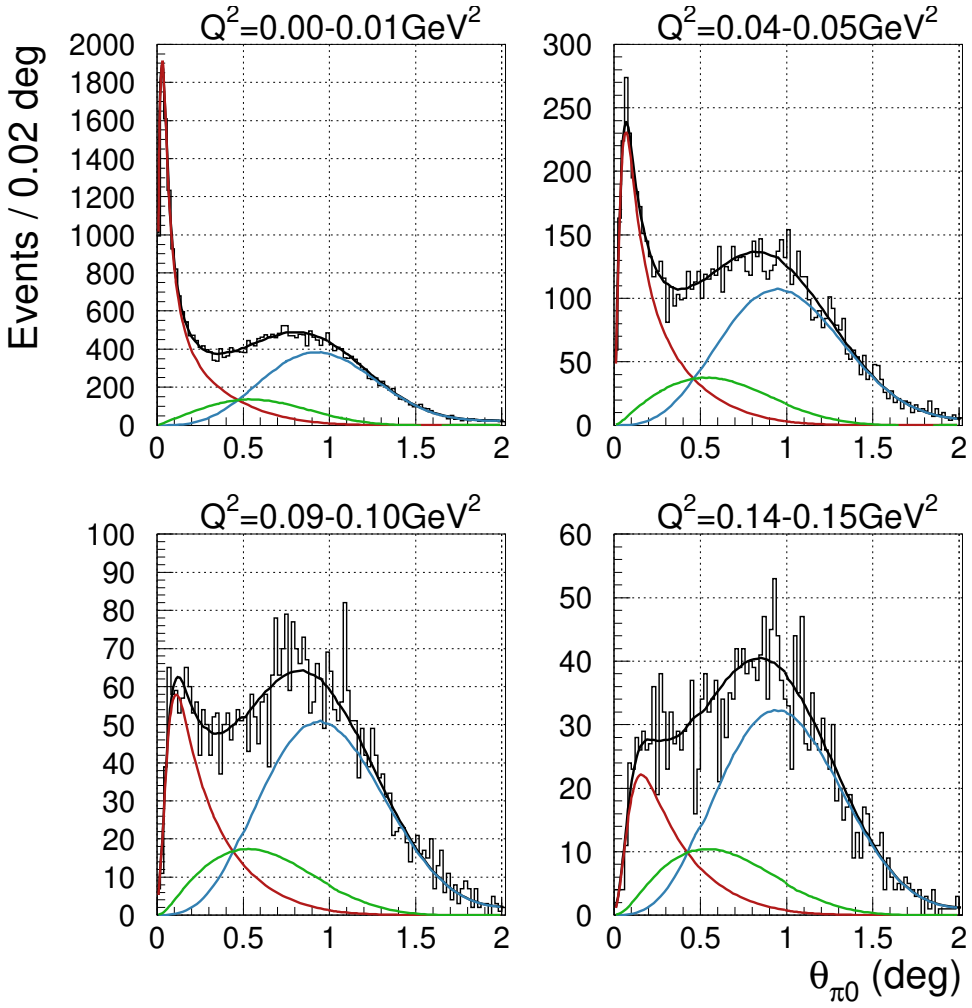

Figure 33: Simulated detected yield for π^0 electroproduction, and Q^2 ranges $0.0-0.01\,\mathrm{GeV}^2$ (top left), $0.04-0.05\,\mathrm{GeV}^2$ (top right), $0.09-0.10\,\mathrm{GeV}^2$ (bottom left), $0.14-0.15\,\mathrm{GeV}^2$ (bottom right). Curves show input from Coulomb (red), strong coherent (blue), and their interference (green) production mechanisms.

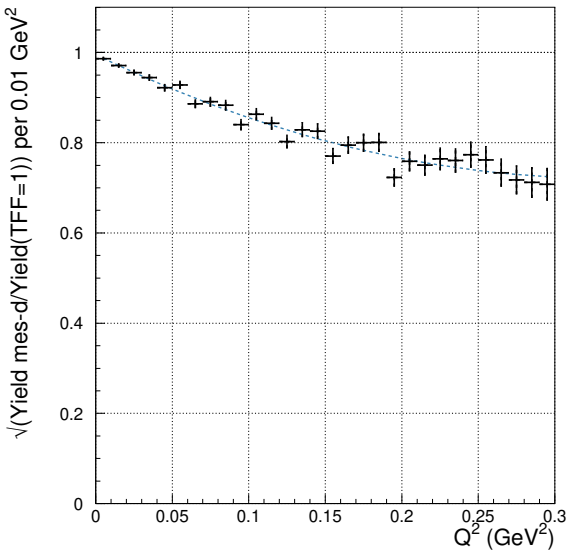

Figure 34: Square root of the realistic yield and yield simulated with the constant TFF=1 ratio split in Q^2 bins. Curve shows fit result.

Given the Q^2 range of the experiment, $Q^2_{max} \approx 0.3$ GeV^2, and the saturation of $a_\mu^{HLbL-\pi^0}$ with increasing Q^2 cutoff (see Fig. 3), we estimate the experiment can constrain $\simeq 65\,\%$ of $a_\mu^{HLbL-\pi^0}$. Due to the low mass of the π^0 relative to the η and η', $a_\mu^{HLbL-\pi^0}$ is the dominant contribution to $a_\mu^{HLbL-pole}$, with $a_\mu^{HLbL-\pi^0}/a_\mu^{HLbL-pole} \simeq 0.67$.

Propagating errors for $\Gamma_{\pi^0\to\gamma\gamma}$, a_π and b_π into the calculation for $a_\mu^{HLbL-\pi^0}$ gives an uncertainty of $\simeq 6\%$ for $a_\mu^{HLbL-\pi^0}$ integrated to $Q^2_{1,2} < 0.3$ GeV^2. This estimate *does not* include uncertainties in the c_π term in Eqn. 1, nor does it include uncertainties in higher order terms in the TFF expansion, which to $O(Q^6)$ goes as,

$$F_{\gamma^*\gamma^*\to\pi^0}(-Q_1^2,-Q_2^2) = \sqrt{\frac{4\Gamma_{\pi^0\to\gamma\gamma}}{\pi\alpha^2 m_\pi^3}}\Big[... + \frac{d_\pi}{m_\pi^6}\Big(Q_1^6+Q_2^6\Big) + \frac{e_\pi}{m_\pi^6}\Big(Q_1^4Q_2^2+Q_1^2Q_2^4\Big) + ...\Big] \quad (13)$$

Because of the limited Q^2 range of the experiment, the data has little sensitivity to the d_π term in Eqn. 13, (inclusion of BES-III data into the fit would improve this sensitivity), and little sensitivity to "cross terms" in the TFF expansion, i.e. c_π and e_π, due to the small range in Mandelstam t for the Primakoff reaction. A model-dependent approach for evaluating $a_\mu^{HLbL-\pi^0}$ is to use the LMD+V TFF [28] to fix the expansion terms unconstrained by experiment. The LMD+V model also predicts relationships between a_π, b_π and c_π, so that by measuring two of the parameters the third can be constrained.

Table 4: LMD+V TFF expansion to $O(Q^6)$. The 3^{rd} column shows the expansion terms, which are dimensionless except in the case of $\Gamma_{\pi^0\to\gamma\gamma}$. The 4^{th} column shows the fractional change in $a_\mu^{HLbL-\pi^0}$ integrated over $Q^2_{1,2} < 0.3$ GeV^2 divided by the fractional change in the LMD+V expansion term.

TFF expansion term	$O(Q^2)$	Term value	$\frac{\Delta a_\mu^{HLbL-\pi^0}}{a_\mu^{HLbL-\pi^0}} / \frac{\Delta term}{term}$
$\Gamma_{\pi^0\to\gamma\gamma}$	1	7.802 eV	1.00
a_π	$O(Q^2)$	.0303	-0.695
b_π	$O(Q^4)$	.000917	0.235
c_π	$O(Q^4)$	.00108	0.106
d_π	$O(Q^6)$	-2.75×10^{-5}	-0.106
e_π	$O(Q^6)$	-3.38×10^{-5}	-0.0577

Table 4 shows the LMD+V TFF expansion to $O(Q^6)$. The 4^{th} column of Table 4 shows the fractional change in $a_\mu^{HLbL-\pi^0}$ integrated over $Q^2_{1,2} < 0.3$ GeV^2 divided by the fractional change in the LMD+V expansion terms. This ratio gives an indication of the *"sensitivity"* of $a_\mu^{HLbL-\pi^0}$ to the expansion terms. Because $a_\mu^{HLbL-\pi^0}$ is proportional to $\Gamma_{\pi^0\to\gamma\gamma}$, the sensitivity of $a_\mu^{HLbL-\pi^0}$ to $\Gamma_{\pi^0\to\gamma\gamma}$ is maximal at 1.0. The sensitivity of $a_\mu^{HLbL-\pi^0}$ to a_π is also very significant, of order unity. Sensitivity to higher order terms drops off significantly.

This analysis clearly demonstrates the need for low-Q^2 experimental data beyond the limited range that is currently available.

To choose the target material we have tested few different nuclei from carbon to lead. One of the requirements is that the main element isotope should be spinless as it simplifies cross section analysis. We kept target thickness in the units of radiation lengths fixed and equal to 250 μm of silicon for this test as Primakoff yield is approximately proportional to this quantity. More heavy nuclei shows reduction in Moller background as it grows linearly with atomic number while the number of atoms decreasing reverse proportionally to atomic number square. More heavy nuclei show significant decrease in the strong coherent production yield as an effect of internal absorption in large nuclei, while the Primakoff production is mostly happens outside of a nucleus in the Coulomb field and not suffered from this effect. At the same time the strong coherent peak in angular distributions for heavy nuclei are shifted closer to the Primakoff peak and became less distinguishable especially for high Q^2 values: the Primakoff peak position is close to the zero production angle value, but strong production peak position is defined by the form factor with the position reverse proportional to the nucleus size. Figures 35-41 show the simulated yield for the tested targets as a function of production angle, for the different Q^2 ranges. The height

Table 5: π^0 TFF parameters uncertainty for different target nuclei, 60 days of 10 nA beam time, and target thickness in radiation length units equivalent to 250 μm of silicon.

Target	Relative uncertainty (stat) [%]		
	$\Gamma(\pi^0 \to \gamma\gamma)$	TFF Slope	TFF Quadrature term
^{12}C	0.36	6.1	16.0
^{28}Si	0.34	5.8	15.4
^{40}Ar	0.34	5.9	15.8
^{98}Mo	0.34	6.0	16.4
^{108}Pd	0.34	6.1	16.5
^{196}Pt	0.34	6.2	17.2
^{208}Pb	0.34	6.2	17.3

of the histograms kept the same for all targets for the convenience. Different production mechanisms shown in different colors.

The extracted Primakoff yields for Q^2 bins from 0 to 0.3 GeV^2 for these targets have been fitted and TFF parameters were extracted. The procedure has been repeated for 100 samples of the simulated data to decrease an error on the obtained uncertainty. Table 5 shows the results for the relative uncertainty of the extracted parameters. Si^{28} shows the minimum of the obtained uncertainty values.

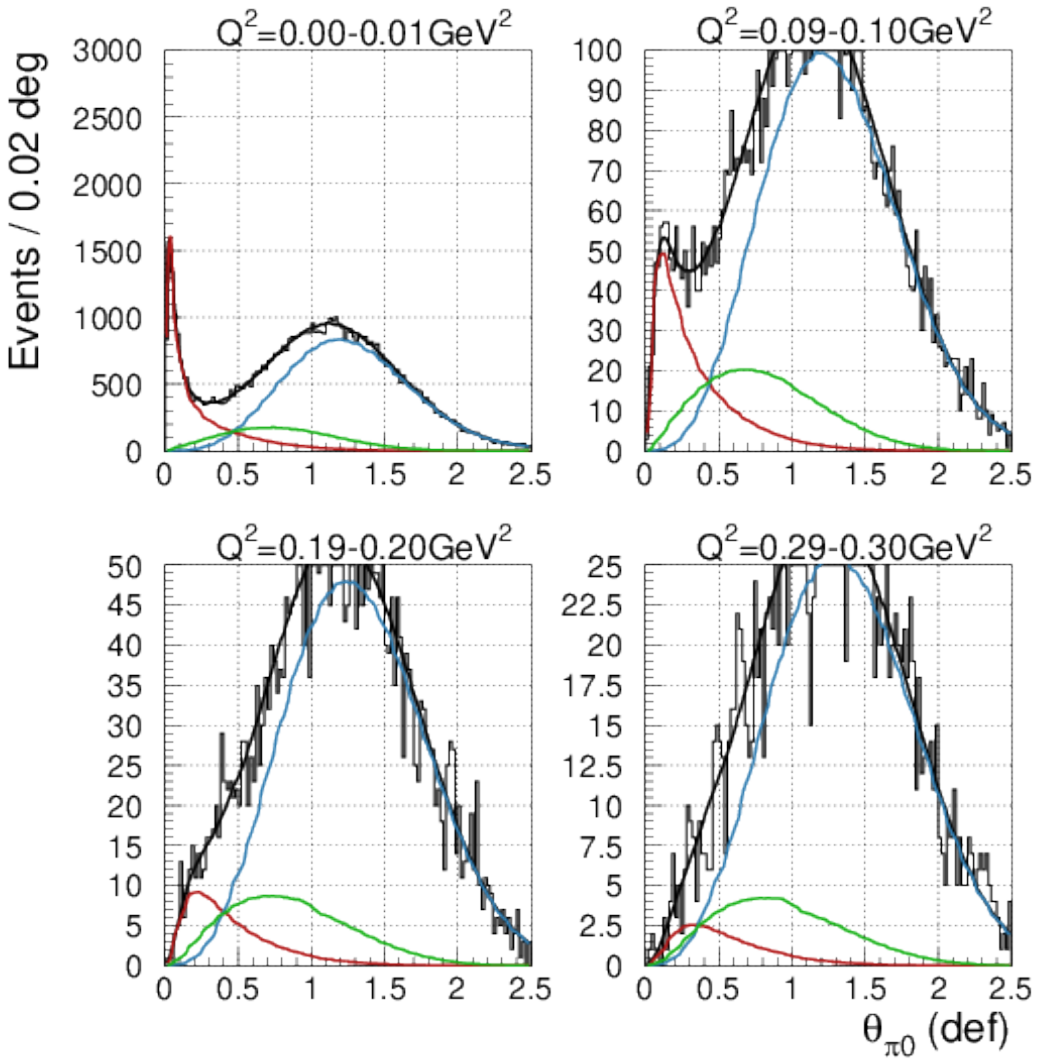

Figure 35: Simulated detected yield for π^0 electroproduction on ^{12}C, and Q^2 ranges 0.0–0.01 GeV^2 (top left), 0.09–0.10 GeV^2 (top right), 0.19–0.20 GeV^2 (bottom left), 0.29–0.30 GeV^2 (bottom right). Curves show input from Coulomb (red), strong coherent (blue), and their interference (green) production mechanisms.

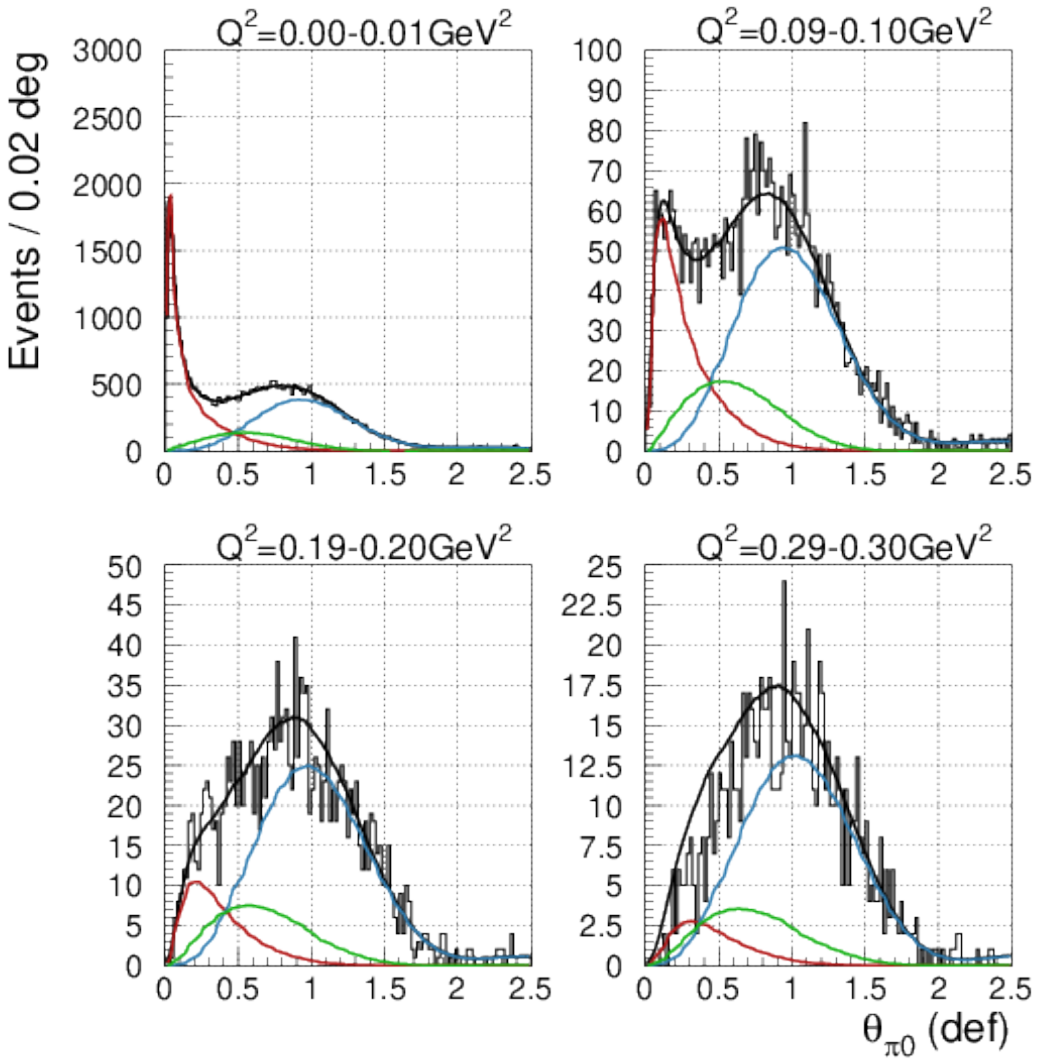

Figure 36: Simulated detected yield for π^0 electroproduction on ^{28}Si, and Q^2 ranges 0.0–0.01 GeV^2 (top left), 0.09–0.10 GeV^2 (top right), 0.19–0.20 GeV^2 (bottom left), 0.29–0.30 GeV^2 (bottom right). Curves show input from Coulomb (red), strong coherent (blue), and their interference (green) production mechanisms.

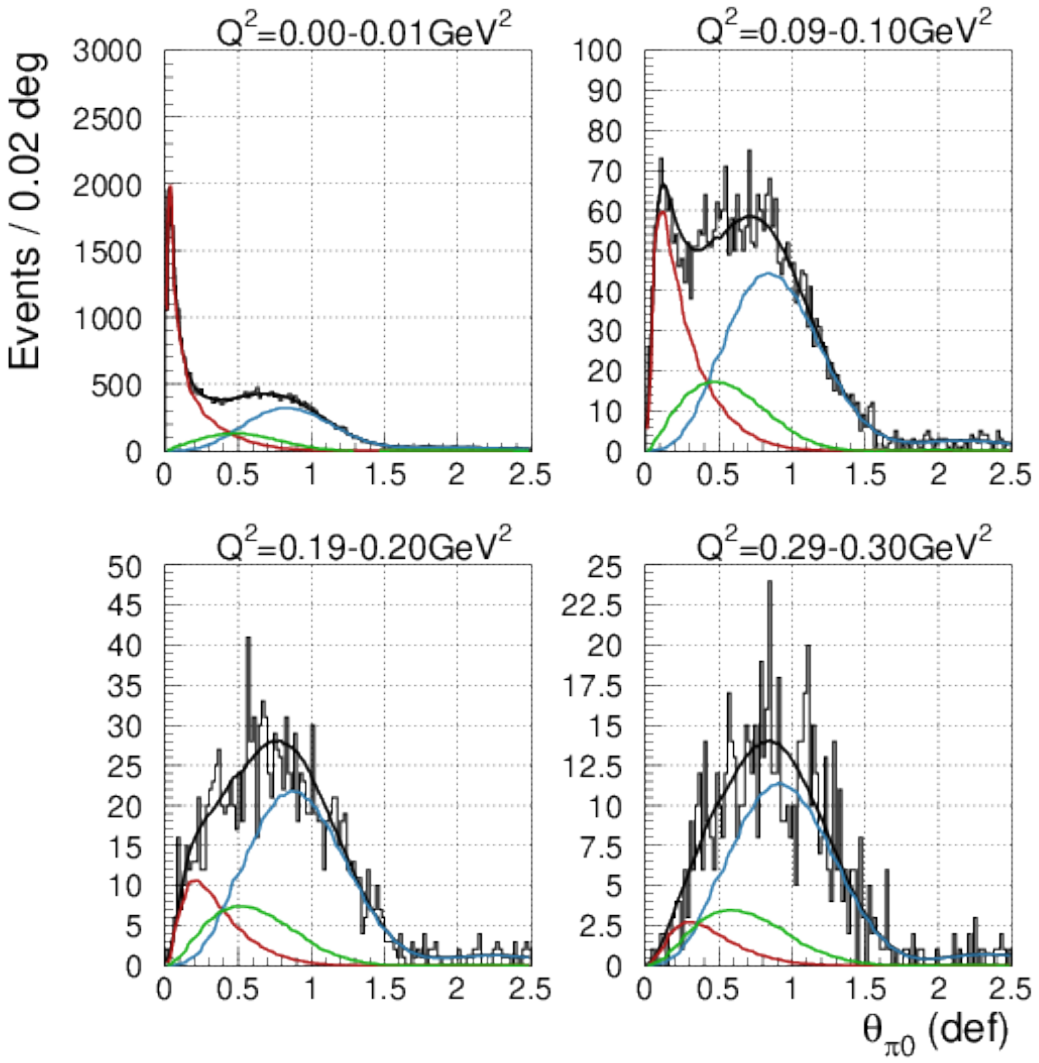

Figure 37: Simulated detected yield for π^0 electroproduction on ^{40}Ar, and Q^2 ranges 0.0–0.01 GeV^2 (top left), 0.09–0.10 GeV^2 (top right), 0.19–0.20 GeV^2 (bottom left), 0.29–0.30 GeV^2 (bottom right). Curves show input from Coulomb (red), strong coherent (blue), and their interference (green) production mechanisms.

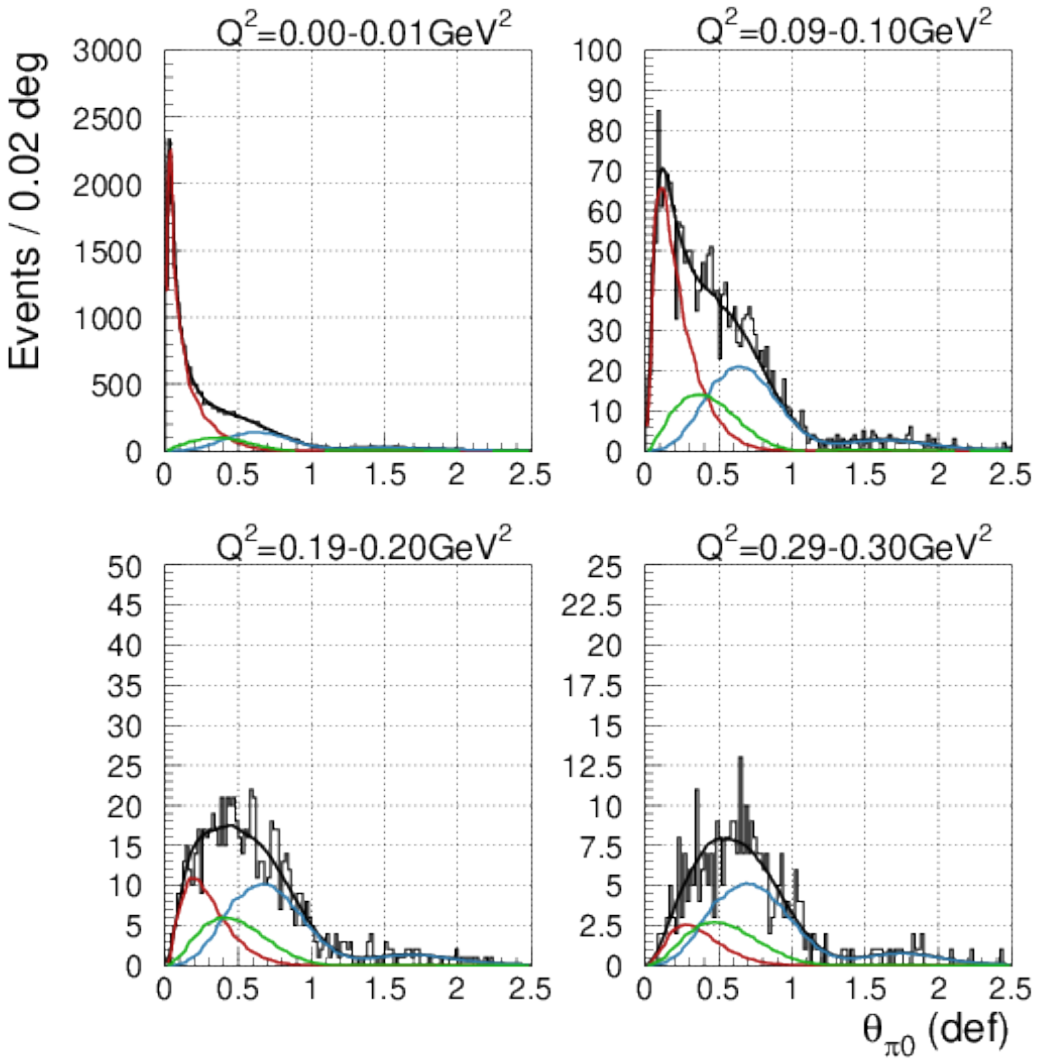

Figure 38: Simulated detected yield for π^0 electroproduction on ^{98}Mo, and Q^2 ranges 0.0–0.01 GeV^2 (top left), 0.09–0.10 GeV^2 (top right), 0.19–0.20 GeV^2 (bottom left), 0.29–0.30 GeV^2 (bottom right). Curves show input from Coulomb (red), strong coherent (blue), and their interference (green) production mechanisms.

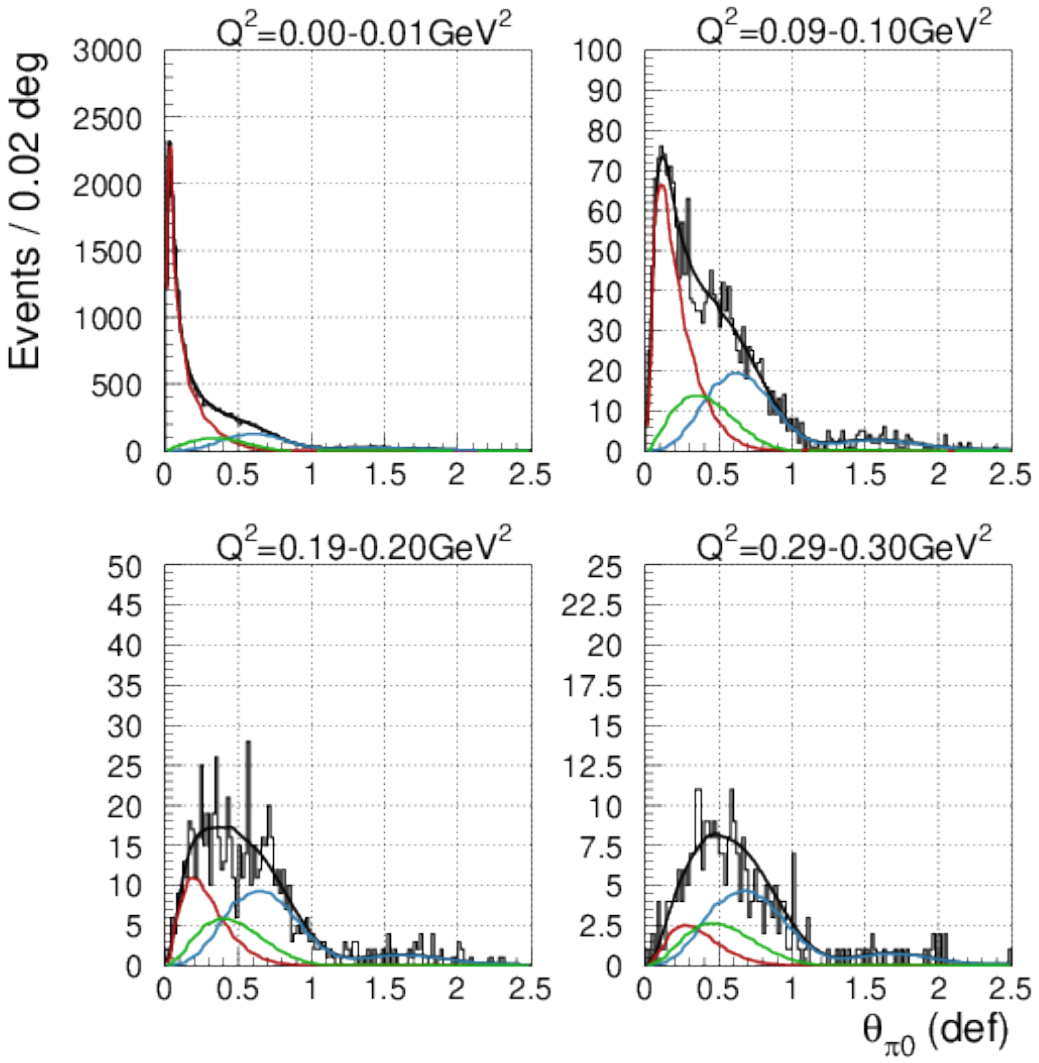

Figure 39: Simulated detected yield for π^0 electroproduction on ^{108}Pd, and Q^2 ranges 0.0–0.01 GeV^2 (top left), 0.09–0.10 GeV^2 (top right), 0.19–0.20 GeV^2 (bottom left), 0.29–0.30 GeV^2 (bottom right). Curves show input from Coulomb (red), strong coherent (blue), and their interference (green) production mechanisms.

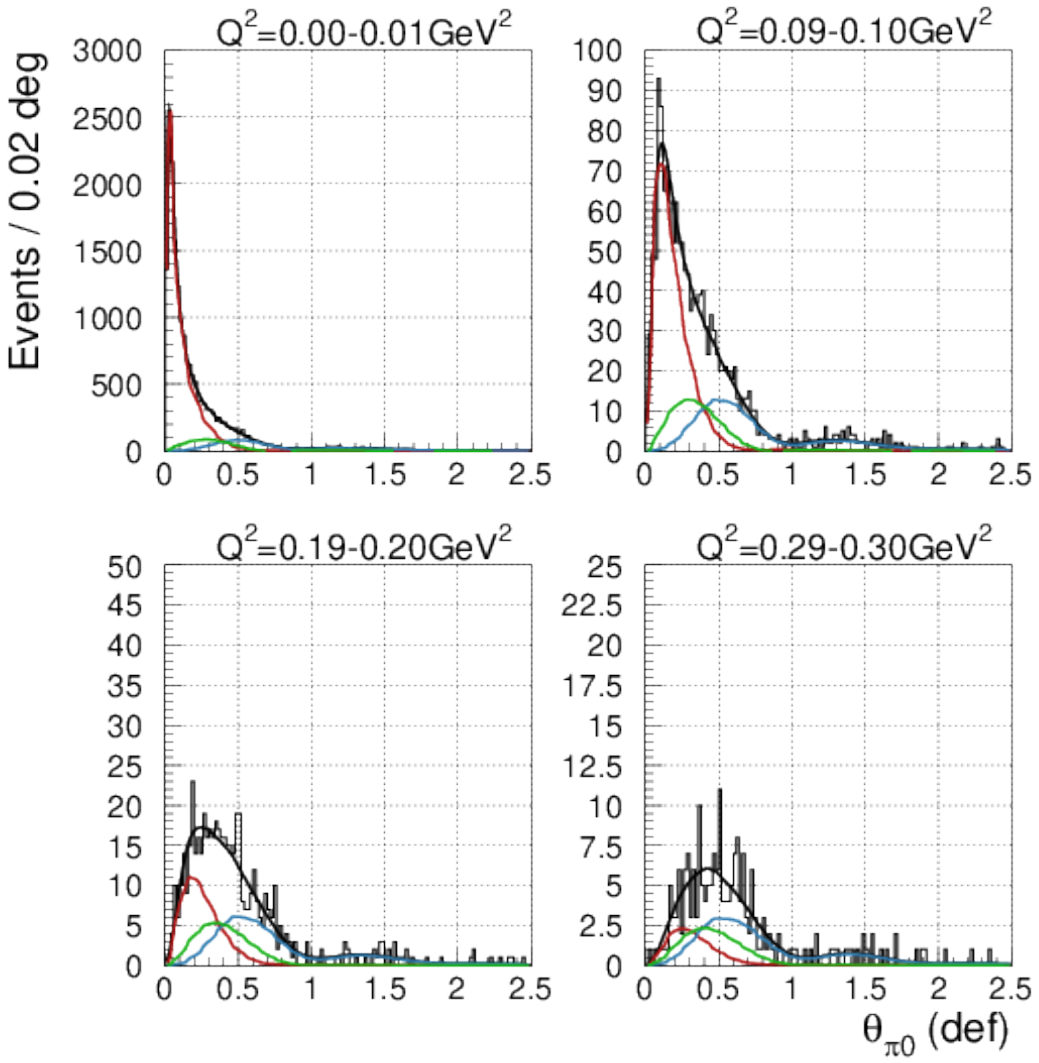

Figure 40: Simulated detected yield for π^0 electroproduction on ^{196}Pt, and Q^2 ranges 0.0–0.01 GeV^2 (top left), 0.09–0.10 GeV^2 (top right), 0.19–0.20 GeV^2 (bottom left), 0.29–0.30 GeV^2 (bottom right). Curves show input from Coulomb (red), strong coherent (blue), and their interference (green) production mechanisms.

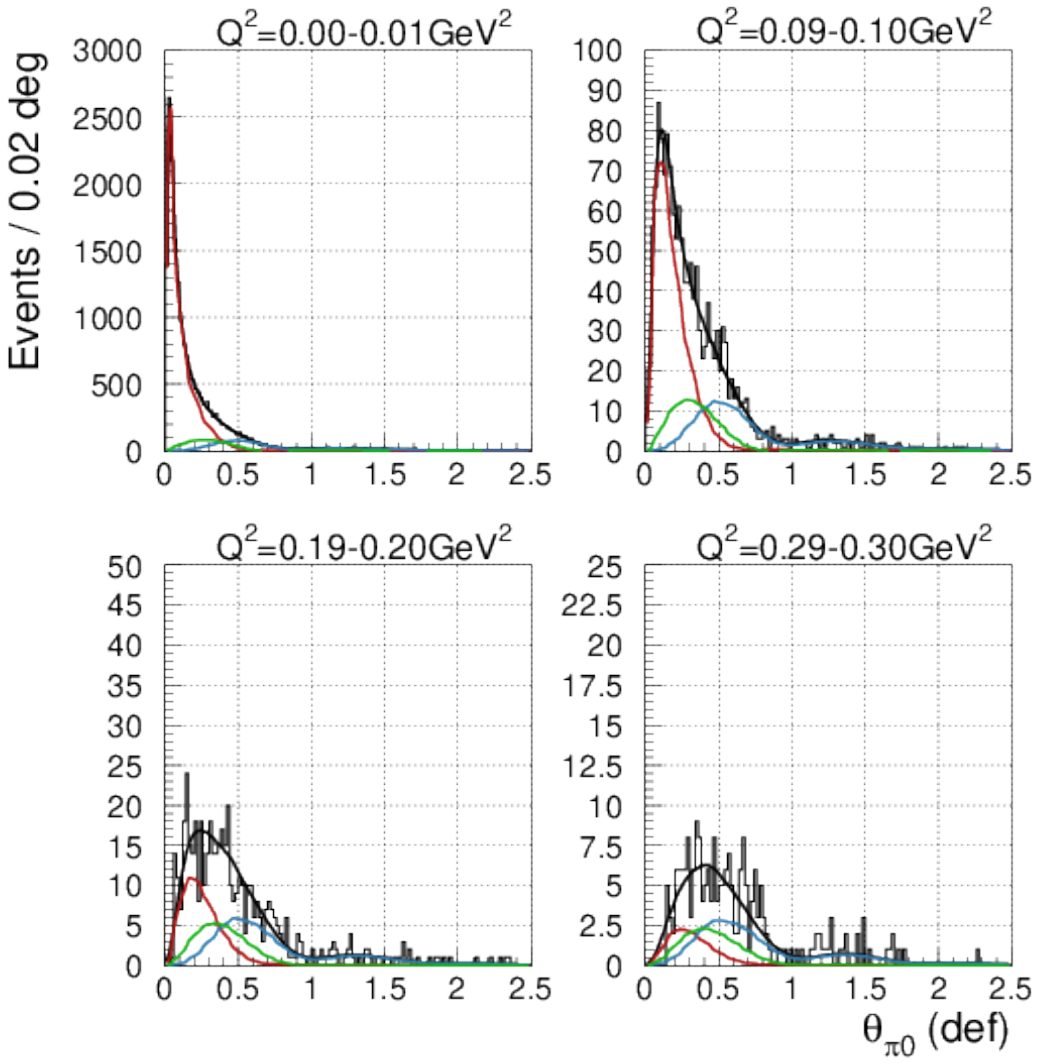

Figure 41: Simulated detected yield for π^0 electroproduction on ^{208}Pb, and Q^2 ranges 0.0–0.01 GeV^2 (top left), 0.09–0.10 GeV^2 (top right), 0.19–0.20 GeV^2 (bottom left), 0.29–0.30 GeV^2 (bottom right). Curves show input from Coulomb (red), strong coherent (blue), and their interference (green) production mechanisms.

Table 6: Beam time request

Experiment phase	Time [days]
Production with silicon target	60
Production with empty target	2
Setup checkout, trigger tests, gain equalization, energy change	5
Total	67

11 Beam time request

With the expected rates we are requesting 60 days of run time for the physics data taking at 10.5 GeV electron beam energy and silicon target to have sufficient statistics for the precise extraction of the neutral pion form factor parameters. We will need 5 more days for setup checkout, tests and gain equalization procedure at 5.5 GeV beam energy, and energy change. We will also need 2 days of running without the target to use this statistics for background subtraction. Table 6 summarizes these numbers.

With that, we are requesting a total of 67 days to perform this experiment and extract the neutral pion transition form factor parameters.

12 Summary of the proposed experiment and its impact on tests of the Standard Model

Measurements of the neutral pion transition form factor (TFF) in the low-Q^2 space-like region can determine two key observables in low-energy strong-interaction physics, (i) the neutral pion radiative width $\Gamma_{\pi^0\to\gamma\gamma}$, predicted by the chiral anomaly, and (ii) the neutral pion transition radius. Measurements of the neutral pion TFF are also very important in constraining and allowing for calculations of the hadronic light-by-light (HLbL) scattering contribution to the muon anomalous magnetic moment.

The measurement of the π^0 TFF through the Primakoff reaction with virtual incident photons will run using the PRad setup in Hall B. Both the scattered electron and the two decay photons will be detected in HYCAL, with GEMs used for electron tracking and background suppression. The proposed measurement has sensitivity to the TFF over a Q^2 range from $0.003\,^2$ to $0.3\,\mathrm{GeV}^2$, allowing a clean determination of the slope and curvature parameters in the TFF, and complementing the space-like BESIII and CELLO measurements at $Q^2 > 0.3\,\mathrm{GeV}^2$, and Dalitz decay measurements in the time-like region.

The JLab fADC-125 system should be used for triggering and data taking. The PRad collaboration has proposed upgrading the HyCal calorimeter to be an all $PbWO_4$ calorime-

ter, rather than the hybrid version. In this upgrade the lead-glass modules would be replaced with new $PbWO_4$ crystals. While this upgrade is welcomed for the proposed TFF measurement, it is not essential.

The $\Gamma_{\pi^0\to\gamma\gamma}$ extraction procedure and experimental setup are very similar to the PrimEx photo-production measurement [1]. Relative to PrimEx, we expect an improvement in the largest contributions to the total PrimEx systematic error: beam flux (electron beam flux measurements have better precision than photon flux measurements), and yield extraction (the PRad vacuum box eliminates downstream beam interactions, which were responsible for the main non-resonant background for Primakoff photo-production in PrimEx). Uncertainties in remaining items in the overall systematic error (neutral pion production theory, acceptance, target, trigger efficiency) have smaller contributions to the overall systematic error, and are expected to be about the same as for PrimEx. Thus we expect the systematic uncertainty in the $\Gamma_{\pi^0\to\gamma\gamma}$ measurement to be approximately 1.4% or better.

The TFF slope and curvature parameters a_π and b_π have projected statistical uncertainties of approximately 6% and 17% respectively for the expected Primakoff yield. Unlike the extraction of $\Gamma_{\pi^0\to\gamma\gamma}$, the extraction of these parameters doesn't require knowledge of the absolute luminosity, and is not affected by its uncertainty. The main experimental contribution here is the detection efficiency uncertainty. The fit of the TFF Q^2 dependence to extract a_π and b_π parameters is also affected by the high order terms in Eq. 1. It is small for $\Gamma(\pi^0 \to \gamma\gamma)$ and has higher values for a_π and b_π. The conservative estimation of the TFF(Q^2) curve interpretation uncertainty is about 2 % and 10 % for a_π and b_π respectively. The expected systematic errors for a_π and b_π are well below the statistical uncertainties. The estimated uncertainty in the slope term a_π corresponds to a 3% error in the neutral pion electromagnetic transition radius.

Table 7 summarizes expected uncertainty contributions. We used PrimEx uncertainty values for the beam flux: a smaller value is anticipated as was already mentioned. We expect the main uncertainty contribution to the target number of atoms from the thickness measurement, which we estimate to be better than 1 μm. For the detection efficiency and acceptance uncertainty the observed in PrimEx value has been increased by factor of 1.5 as we now detecting 3 particles in the final state (2 particles were detected in PrimEx). The main contribution to the event selection uncertainty arises from the energy selection for the scattered electron. In PrimEx it was only 0.5 GeV minimum energy requirement, and here we have both minimum (0.5 GeV) and maximum (4.5 GeV) energy selection, thus this value is taken as doubled corresponding PrimEx value. In yield extraction systematics we expect a major improvement from eliminating beam interactions downstream the target. We have taken here the PrimEx value corresponding to the reduced non-resonant background level corresponding to observed in PrimEx "empty target" background. The trigger efficiency will be measured using prescaled random and calorimeter total energy trigger data. It has very small uncertainty and was successfully utilized by PrimEx. The uncertainty coming from the extraction of the Primakoff part from the total cross section with assumes known cross section shape and utilizes the theory is the same as in the PrimEx measurement. The

Table 7: Expected measurement uncertainty budget

Item	Value [%]		
Measured value	$\Gamma(\pi^0 \to \gamma\gamma)$	TFF slope parameter	TFF Quadrature term
Beam flux	0.8	none	
Target thickness	0.4	none	
Setup acceptance and detection efficiency	0.7		
Event selection	0.4		
Yield extraction	0.7		
Trigger efficiency	0.1		
π^0 production theory parameters	0.4		
radiative corrections	< 0.1		
High order terms (Eq. 1) in TFF Q^2-dependence fit	0.1	2	10
Total systematics	1.4	2.4	10
Statistical	0.7	6	17
Total	1.6	6.5	20

effect of radiative corrections is estimated in the Appendix C.1. The whole effect has level of 0.4 %, and its expected uncertainty is below 0.1 %. The estimated values of uncertainties originating from high order terms (Eq. 1) are added to the table as a stand alone item.

We conclude by noting that FNAL E989 may soon reach the 5σ "gold standard" for discovery of physics beyond the Standard Model. Given the importance of this possible discovery, we believe existing experimental constraints, *based on a relatively meager coverage of the low-Q^2 region*, of the π^0 TFF are inadequate for a precision measurement of the π^0-pole contribution to HLbL – the largest single component of HLbL. By measuring the π^0 TFF over the region $Q^2 \approx 0.003$ to $0.3\,\mathrm{GeV}^2$ where no data currently exists, the proposed experiment will constrain approximately 65 % of the π^0-pole contribution to HLbL. The projected Q^2 range the projected uncertainties are shown in Fig. 42. The projected errors in $\Gamma_{\pi^0\to\gamma\gamma}$, a_π, and b_π give an estimated uncertainty of 6 % in the π^0-pole contribution to HLbL integrated to $Q^2 = 0.3$ GeV^2. The list of observables and their projected uncertainties are shown in Table. 8.

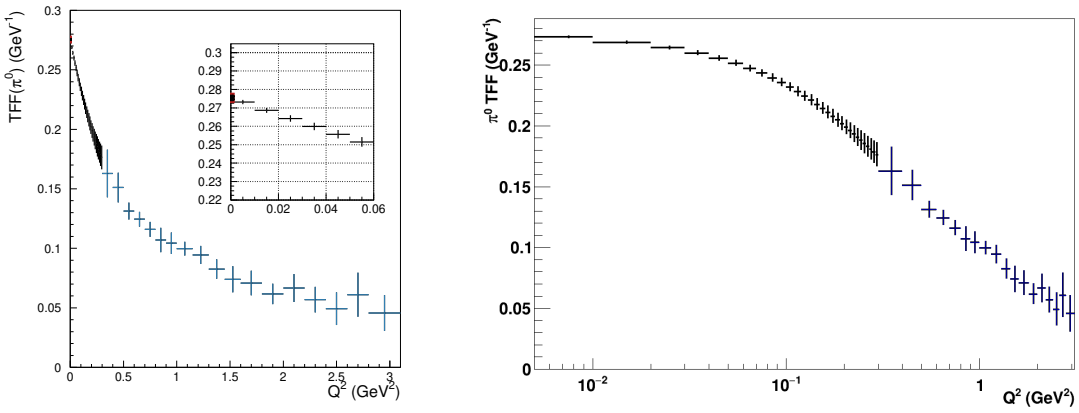

Figure 42: Momentum dependence of the π^0 TFF. Preliminary data from BESIII[3] (blue histogram), PrimEx measurement (red point at $Q^2 = 0$, left panel only), and the projected proposed measurement (black histogram). Q^2 in linear scale (left) and log scale (right).

Table 8: Projected uncertainty for this proposal compared to current status.

Measured quantity	Current status of uncertainty	This proposal
TFF(π^0) $F(Q^2)$	10 - 25 % (for $Q^2 \approx$ 0.3 - 3.8 GeV^2)	0.4 - 8 % (for $Q^2 \approx$ 0.003 - 0.3 GeV^2)
TFF Slope (a_π)	9%	6%
TFF curvature (b_π)	unmeasured	17%
RMS transition radius ($< r^2_{\pi^0} >^{1/2}$)	5%	3%
Decay width ($\Gamma_{\pi^0 \to \gamma\gamma}$)	1.3%	1.4 %
HLbL π^0-pole ($a_\mu^{HLbL-\pi^0}$)	4% †	6%

† Estimated theoretical uncertainty [14]

A Strong π^0 electroproduction

In this section we present S. Gevorkyan's calculation of strong π^0 electroproduction from nuclear targets.

The neutral pion can be produced in a coherent nuclear photoproduction process via the ω and ρ meson exchanges. The nuclear coherent electroproduction amplitude reads [35]:

$$M(eA \to e\pi^0 A) = j_\mu(q)\frac{-i}{q^2}J_\mu(t) \tag{14}$$

where the lepton current $j_\mu(q) = i\,e\bar{u}(k_2)\gamma_\mu u(k_1)$ is the amplitude of photon radiation by

electron $e \to e'\gamma$, whereas the hadronic current $J_\mu(t)$ is proportional to the vector product $[\vec{q} \times \vec{k}_\pi]$. k_1, k_2, k_π, q, and t are 4-momenta of beam electron, scattered electron, pion, virtual photon beam, and Coulomb photon transferred to a nucleus correspondingly. The amplitude of π^0 photoproduction is a product of hadronic current and Coulomb photon polarization $M(\gamma A \to \pi^0 A) = \vec{\epsilon}\vec{J}(t)$. Thus to transfer from photoproduction to electroproduction it is enough to change the photon polarization vector with the lepton current. The contribution from ω exchange to the π^0 photoproduction amplitude on nucleon reads [35]:

$$M(\gamma N \to \pi^0 N) = i\, e\, \frac{g_{\omega\pi\gamma}}{m_\pi} g_{\omega NN}\, R_\omega\, \vec{\epsilon}[\vec{q} \times \vec{k}_\pi]\, 2m_N \tag{15}$$

The contribution from ρ exchange is proportional to the difference between number of neutrons and protons $(N-Z)$ as the amplitudes of the photoproduction on proton and neutron by ρ exchange have opposite signs due to isospin one. Thus for symmetric nucleus its contribution is zero. Nevertheless for heavy nuclei such as lead it can be essential and we add it here. As a result the strong coherent cross section has the form:

$$\frac{d^3\sigma_S}{dE_2 d\Omega_2 \Omega_\pi} = \frac{\sigma_M Q^4}{\pi m_\pi^2} \frac{\beta_\pi^- 1}{E_\pi} |F_N(t)|^2 E_1 E_2 sin^2 \frac{\theta_e}{2} sin^2\theta_\pi\, |AL_\omega + (Z-N)L_\rho|^2 \tag{16}$$

$$L_\omega = \frac{g_{\omega\pi\gamma} g_{\omega NN}}{4\pi} R_\omega; \qquad L_\rho = \frac{g_{\rho\pi\gamma} g_{\rho NN}}{4\pi} R_\rho \tag{17}$$

Here we use the same notations as in Equation 3, and relevant constants g and R are described in [35].

The incoherent π^0 electroproduction cross section can be calculated using connection between the process $e(k_1)+A(p_1) \to e(k_2)+\pi^0(k)+A'(p_2)$ and the incoherent process of π^0 production off nucleus by real photon $\gamma(q) + A \to \pi^0(k) + A'$ [36]: $\frac{d\sigma^{inc}}{dE_2 d\Omega_2 d\Omega_\pi} = \Gamma \times \frac{d\sigma^{inc}}{d\Omega_\pi}$, where $\Gamma = \frac{\alpha}{2\pi^2} \frac{E_2}{E_1} \frac{|\vec{q}|}{Q^2} \frac{1}{1-\epsilon}$, $\epsilon = 1\,/\,(1 + 2\,\frac{|\vec{q}|^2}{Q^2} tan^2(\theta_e/2))$. The effects of the electron-photon vertex and the photon propagator are contained in the electrodynamics term Γ. The incoherent photoproduction cross section term $\frac{d\sigma^{inc}}{d\Omega_\pi}$ is similar to the equation 27 in [37].

B Pseudo-scalar pole contribution to $(g-2)_\mu$

In this section we present results relating to the pion pole contribution to HLbL, and the workings of the code used to calculate $a_\mu^{\text{HLbL:}\pi^0}$. The requirements to run the code are:

- C++
- CERN Root
- GSL
- Make

B.1 Background

Our ultimate goal is to calculate the pseudoscalar pion-pole contribution $a_\mu^{\text{HLbL:}\pi^0}$, which can be found through the following equation:

$$a_\mu^{\text{HLbL:}\pi^0} = \left(\frac{\alpha}{\pi}\right)\left[a_\mu^{\text{HLbL:}\pi^0(1)} + a_\mu^{\text{HLbL:}\pi^0(2)}\right]$$

where α is the fine structure constant. The two terms on the right both have triple integral representations:

$$a_\mu^{\text{HLbL:}\pi^0(1)} = \int_0^\infty dQ_1 \int_0^\infty dQ_2 \int_{-1}^1 d\tau w_1(Q_1,Q_2,\tau)\mathcal{F}_{\pi^0\gamma^*\gamma^*}(-Q_1^2,-(Q_1{+}Q_2)^2)\mathcal{F}_{\pi^0\gamma^*\gamma^*}(-Q_2^2,0) \tag{18}$$

$$a_\mu^{\text{HLbL:}\pi^0(2)} = \int_0^\infty dQ_1 \int_0^\infty dQ_2 \int_{-1}^1 d\tau w_2(Q_1,Q_2,\tau)\mathcal{F}_{\pi^0\gamma^*\gamma^*}(-Q_1^2,-Q_2^2)\mathcal{F}_{\pi^0\gamma^*\gamma^*}(-(Q_1{+}Q_2)^2,0) \tag{19}$$

where w_1 and w_2 are weighting functions:

$$w_1(Q_1,Q_2,\tau) = \left(\frac{-2\pi}{3}\right)\sqrt{1-\tau^2}\frac{Q_1^3Q_2^3}{Q_2^2+m_\pi^2}I_1(Q_1,Q_2,\tau)$$

$$w_2(Q_1,Q_2,\tau) = \left(\frac{-2\pi}{3}\right)\sqrt{1-\tau^2}\frac{Q_1^3Q_2^3}{(Q_1+Q_2)^2+m_\pi^2}I_2(Q_1,Q_2,\tau)$$

The definitions of I_1 and I_2 are quite complex, so they are omitted for now. Their exact definitions can be found in the equation appendix at the end of this document, as well as a table of all relevant constants.

The following figure contains plots of the weighting functions with various fixed values of Q_1 and Q_2 while varying τ (note that the y-axis on the right plot is logarithmic):

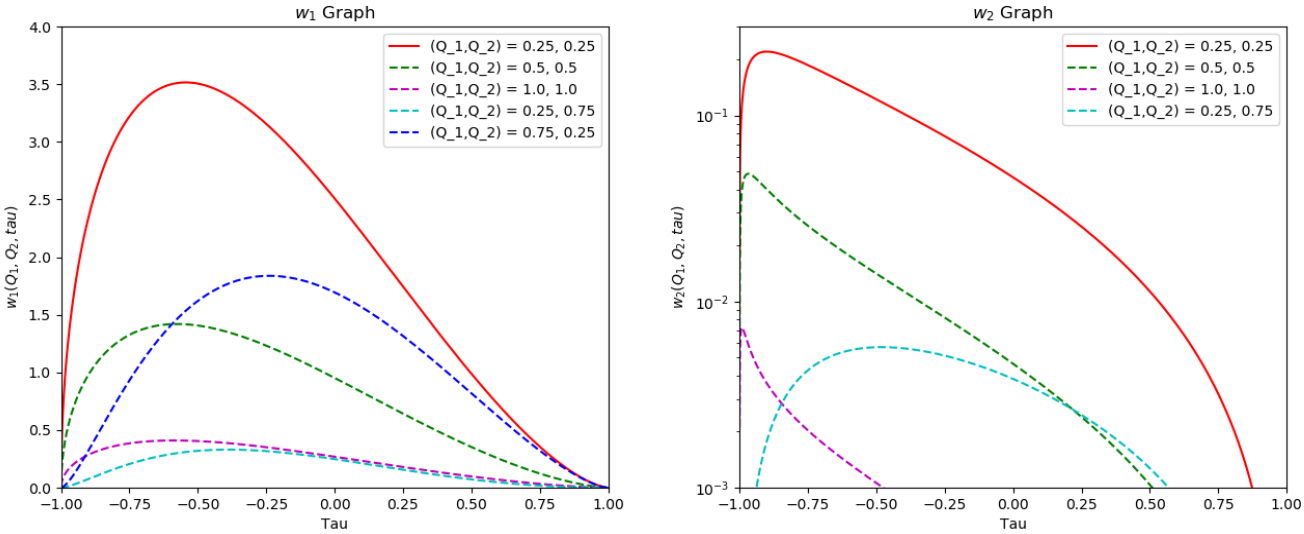

The integrals also involve the on-shell transition form factor for the pion. In particular, we need the lowest meson dominance plus vector parameterization, or LMD+V form factor:

$$\mathcal{F}^{\text{LMD+V}}_{\pi^0\gamma^*\gamma^*}(q_1^2, q_2^2) = \frac{F_\pi}{3} \frac{q_1^2 q_2^2 (q_1^2 + q_2^2) + h_2 q_1^2 q_2^2 + h_5 q_1^2 q_2^2 + h_5 (q_1^2 + q_2^2) + h_7}{(q_1^2 - M_{V_1}^2)(q_1^2 - M_{V_2}^2)(q_2^2 - M_{V_1}^2)(q_2^2 - M_{V_2}^2)} \tag{20}$$

Descriptions of all relevant constants can be found at the end of the document.

B.2 Pion-Pole Contribution Calculations

In order to calculate the pion pole contribution, we must first compute two triple integrals. Of course, it would be impossible to do this by hand given the complexity of the integrands, so we resort to numerical methods. The standard Riemann sum or trapezoid rule algorithms are not be the best course of action however, since as the number of dimensions d in an integral increases they run in $\mathcal{O}(n^d)$. A better algorithm would be Monte Carlo integration, which runs in $\mathcal{O}(n)$ regardless of the number of dimensions, making it well-suited for high-dimensional integrals. Monte Carlo integration works by evaluating the integrand at random points in the domain of integration in order to compute the average value of the function over the domain. This number is then multiplied by the "volume" of the domain of integration to produce the final result. A naive algorithm uses uniform sampling over the whole domain, while more sophisticated algorithms such as MISER and VEGAS use stratified and importance sampling to place samples in areas which decrease the overall variance of the result.

Although the upper bounds of integration on Q_1 and Q_2 are both ∞, we do not need to integrate out this far in practice to get an accurate result. Both of the weighting functions

approach 0 as $Q_1, Q_2 \to \infty$, so a much smaller upper bound of 20 can be used.

For implementation, GSL provides many optimized Monte Carlo integration algorithms in C++. Using the VEGAS algorithm with 40 million samples and a momentum cutoff of 20, we obtain the result

$$a_{\mu:\mathrm{LMD+V}}^{\mathrm{HLbL}:\pi^0} = 62.9201422692142 \times 10^{-11}$$

which agrees with the value calculated by Nyffeler of 62.9×10^{-11}.

B.3 Low Momentum Expansion

Another topic of interest is the low momentum form factor expansion, which approximates the LMD+V form factor for sufficiently small Q_1 and Q_2. The Q^6 expansion is:

$$\begin{aligned}\mathcal{F}_{Q^6}(-Q_1^2, -Q_2^2) = \frac{1}{4\pi^2 F_\pi}\big[1 - a(Q_1^2 + Q_2^2) + b(Q_1^4 + Q_2^4) + cQ_1^2Q_2^2 \\ + d(Q_1^6 + Q_2^6) + e(Q_1^4Q_2^2 + Q_1^2Q_2^4) + \cdots\big]\end{aligned} \tag{21}$$

This expansion is valid in the region $Q_1^2 < 0.1,\ Q_2^2 < 0.1$. Below is a graph of the LMD+V form factor along with the Q^4 and Q^6 expansions.

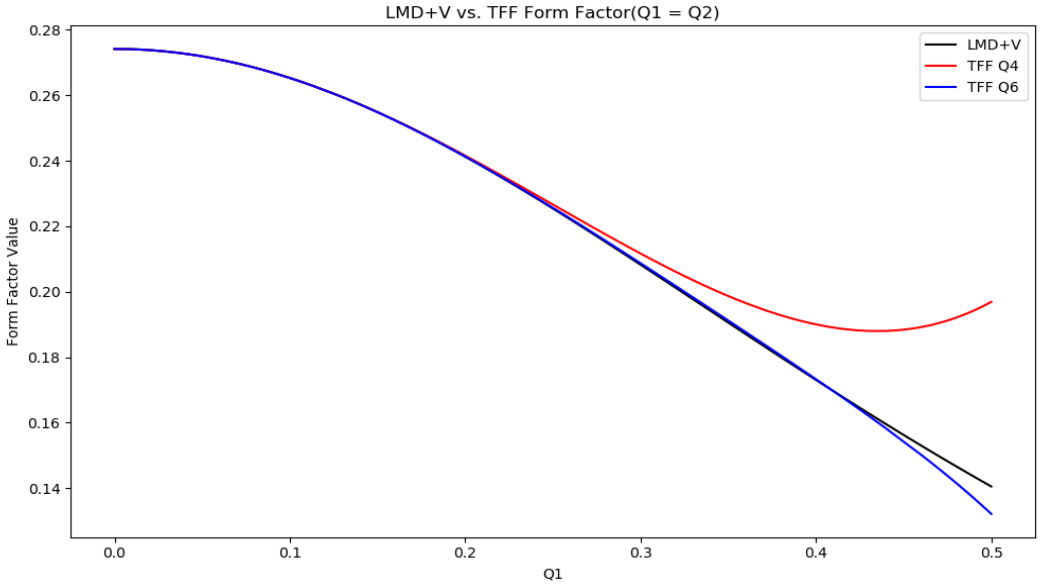

The two expansions are quite accurate in low momentum regions. We can obtain a measure of how accurate they are by performing the integrals in equations (1) and (2) and calculating $a_\mu^{\mathrm{HLbL}:\pi^0}$ using a small momentum cutoff of $Q_{1,2} < 0.1$. The following result used 40 million samples per integral:

```
Integration to Q < 0.1 with 40,000,000 samples
Integral 1 (LMD+V):     0.001005460894  Sigma: 1.864345197e-08
Integral 2 (LMD+V):     0.0001717746828 Sigma: 4.577028494e-09

Integral 1 (Q4)   :     0.001005481982  Sigma: 1.832570684e-08
Integral 2 (Q4)   :     0.000171768857  Sigma: 4.722432529e-09

Integral 1 (Q6)   :     0.001005465541  Sigma: 1.846705857e-08
Integral 2 (Q6)   :     0.0001717705784 Sigma: 4.358205314e-09

Final LMD+V       :     1.475399897e-11
Final Q4          :     1.475419025e-11
Final Q6          :     1.475400577e-11


% Error Q4 = 0.001296464429
% Error Q6 = 4.605865611e-05
```

The percent error is extremely small, so we can be confident that these expansions accurately model the LMD+V form factor. Even when we integrate out to the $Q < 0.55$ region, the Q^6 expasion is still reasonably accurate:

```
Integration to Q < 0.55 with 40,000,000 samples
Integral 1 (LMD+V):     0.03059591231   Sigma: 1.143014661e-06
Integral 2 (LMD+V):     0.001228622807  Sigma: 7.092076856e-08

Integral 1 (Q4)   :     0.03445752339   Sigma: 1.29445538e-06
Integral 2 (Q4)   :     0.001255706317  Sigma: 7.560896752e-08

Integral 1 (Q6)   :     0.0292823835    Sigma: 1.31088181e-06
Integral 2 (Q6)   :     0.001222610122  Sigma: 7.34236183e-08

Final LMD+V       :     3.98848937e-10
Final Q4          :     4.475849735e-10
Final Q6          :     3.823114535e-10


% Error Q4 = 12.21917171
% Error Q6 = 4.146302504
```

Additionally, we are interested in the parameters a, b, c, d, e, and the constant $\Gamma_{\pi^0 \to \gamma\gamma'}$. We can find the uncertainty in these values by calculating the partial derivatives of the

pseudoscalar pion pole contribution $a_\mu^{\mathrm{HLbL};\pi^0}$ with respect to each parameter. We can do this by by using the standard two-sided finite difference algorithm for derivatives:

Let $f : \mathbb{R}^6 \to \mathbb{R}$ be a function that takes the parameters $a, b, c, d, e, \Gamma_{\pi^0 \to \gamma\gamma'}$ as input and outputs the value of the pseudoscalar pion pole contribution using the Q^6 form factor expansion. If we wanted to find the uncertainty in a, for example, we would need to calculate $\dfrac{\partial f}{\partial a}$, which using the two-sided finite differnce is:

$$\frac{\partial f}{\partial a} \approx \frac{f\big(a(1+p), b, c, d, e, \Gamma\big) - f\big(a(1-p), b, c, d, e, \Gamma\big)}{2ap}$$

where $0 < p << 1$ is some small percent offset. In this case, we would choose all parameter values to be their mean value, as in the table of constants. Ideally we want p to be as small as possible, but due to the limitations of floating point arithmetic if p is too small we introduce floating point errors into the calculation. On the other hand, if p is too large the approximation of the partial derivative becomes less valid. In an attempt to mitigate these errors, we will calculate the partials for each parameter for a range of percent offsets and compare them to see if they agree. We find:

```
Integration up to Q < 0.32 with 10,000,000 samples

Partials - parameters varied by 0.25%
a     :       -3.3649414139212751e-11
b     :       6.5597577850400077e-13
c     :       7.5336493834179759e-13
d     :       -2.2389899845111552e-14
e     :       -2.5921871988282577e-13
gamma :       0.028048597506709651

Partials - parameters varied by 0.5%
a     :       -3.4449383778532745e-11
b     :       3.4142804377747982e-12
c     :       8.8450944603176724e-13
d     :       2.8415787365649684e-15
e     :       -9.0179242866092002e-14
gamma :       0.028048597506709985
```

```
Partials - parameters varied by 0.75%
a     :       -3.3191362216371211e-11
b     :       2.5755926746937237e-12
c     :       8.9698494346664814e-13
d     :       5.5273532206700047e-13
e     :       1.1963893088477835e-13
gamma :       0.028048597506711213

Partials - parameters varied by 1%
a     :       -3.2643828344676348e-11
b     :       2.7937088821432139e-12
c     :       7.6711187905363668e-13
d     :       2.4753257230670531e-13
e     :       3.3237715190804097e-14
gamma :       0.028048597506710987

Partials - parameters varied by 2%
a     :       -3.3252659401737983e-11
b     :       2.5268070693977975e-12
c     :       8.0415729114617521e-13
d     :       6.3470922586978126e-14
e     :       3.0352326917181194e-14
gamma :       0.028048597506710987
```

We see that the parameters a, b, and Γ have good agreement, while c, d, and e have less agreement. Increasing the integration bound to $Q < 0.55$ results in better agreement among all parameters:

```
Integration up to Q < 0.55 with 10,000,000 samples

Partials - parameters varied by 0.5%
a       :       -1.64032569337445e-10
b       :       3.38827807205793e-11
c       :       1.14428571606979e-11
d       :       9.08712120200189e-12
e       :       4.35623158169835e-12
gamma   :       0.0494522072073776

Partials - parameters varied by 1%
a       :       -1.64967438673216e-10
b       :       3.24854023731518e-11
c       :       1.1522291345106e-11
```

```
d       :       9.46112561685376e-12
e       :       3.93324334449662e-12
gamma   :       0.0494522072073796

Partials - parameters varied by 2%
a       :       -1.63683649020039e-10
b       :       3.33407981304216e-11
c       :       1.26548343516877e-11
d       :       9.09222852041125e-12
e       :       4.04912057232516e-12
gamma   :       0.0494522072073795
```

B.4 Code Documentation

The subsections here detail what each file does as well as how to compile and run them. The files themselves are also documented with comments in the code. There are 5 files in total:

- functions.h
- main.cpp
- error.cpp
- propagate.cpp
- Makefile

B.4.1 functions.h

This file defines the functions and physical constants needed in the HLbL calculation. Such functions include the form factors and weighting functions.

B.4.2 main.cpp

This program calculates the value $a_\mu^{\mathrm{HLbL}:\pi^0}$. It does this using the VEGAS Monte Carlo integration algorithm (implemented by GSL) to calculate the relevant integrals.

B.4.3 error.cpp

This program calculates the percentage error of the Q^4 and Q^6 form factor expansions. The upper integration bounds on Q_1 and Q_2 can be changed by altering the value of the `limit` variable, and the number of samples used in the integration algorithm can be changed with the `calls` variable. Since a total of 6 integrals need to be calculated, the MISER algorithm (implemented in GSL) is used because it is faster than the VEGAS algorithm.

B.4.4 propagate.cpp

This program computes the partial derivatives of $a_\mu^{\mathrm{HLbL};\pi^0}$ with respect to the parameters a, b, c, d, e, and Γ using the Q^6 expansion. The MISER algorithm is used here since many integrals need to be calculated. The number of samples can be changed by changing the `samples` variable, and the integration bound can be changed with the `cutoff` variable.

B.4.5 Compiling and Running

To compile all of the code, simply run the command `make` in the same directory as the Makefile using the command line. This should generate several files. The important ones are `main`, `error`, and `propagate` (note that these files don't have extensions since they are executables). To run the relevant program, type `./<fileName>` into the command line. For example, to run `main.cpp`, type `./main` into the command line. To remove all of the generated files, run `make clean`. This will not affect any of the source files.

B.5 Weighting functions and form factors

The functions involved in the calculations are quite complicated, so the details are provided here.

B.5.1 Weighting Functions

$$w_1(Q_1,Q_2,\tau)=\left(\frac{-2\pi}{3}\right)\sqrt{1-\tau^2}\,\frac{Q_1^3Q_2^3}{Q_2^2+m_\pi^2}I_1(Q_1,Q_2,\tau)$$

$$w_2(Q_1,Q_2,\tau)=\left(\frac{-2\pi}{3}\right)\sqrt{1-\tau^2}\,\frac{Q_1^3Q_2^3}{(Q_1+Q_2)^2+m_\pi^2}I_2(Q_1,Q_2,\tau)$$

$$\begin{aligned}I_1(Q_1,Q_2,\tau)=X(Q_1,Q_2,\tau)\big[&8P_1P_2(Q_1\cdot Q_2)-2P_1P_3(Q_2^4/m_\mu^2-2Q_2^2)+4P_2P_3Q_1^2-4P_2\\&-2P_1(2-Q_2^2/m_\mu^2+2(Q_1\cdot Q_2)/m_\mu^2)-2P_3(4+Q_1^2/m_\mu^2-2Q_2^2/m_\mu^2)+2/m_\mu^2\big]\\&-2P_1P_2(1+(1-R_{m1})(Q_1\cdot Q_2)/m_\mu^2)+P_1P_3(2-(1-R_{m1})Q_2^2/m_\mu^2)\\&+P_2P_3(2+(1-R_{m1})^2(Q_1\cdot Q_2)/m_\mu^2)+P_1(1-R_{m1})/m_\mu^2+3P_3(1-R_{m1})/m_\mu^2\end{aligned}$$

$$\begin{aligned}I_2(Q_1,Q_2,\tau)=X(Q_1,Q_2,\tau)\big[&4P_1P_2(Q_1\cdot Q_2)+2P_1P_3Q_2^2-2P_1+2P_2P_3Q_1^2-2P_2-4P_3-4/m_\mu^2\big]\\&-2P_1P_2-3P_1(1-R_{m2})/(2m_\mu^2)-3P_2(1-R_{m1})/(2m_\mu^2)-P_3(2-R_{m1}-R_{m2})/(2m_\mu^2)\\&+P_1P_3(2+3(1-R_{m2})Q_2^2/(2m_\mu^2)+(1-R_{m2})^2(Q_1\cdot Q_2)/(2m_\mu^2))\\&+P_2P_3(2+3(1-R_{m1})Q_1^2/(2m_\mu^2)+(1-R_{m1})^2(Q_1\cdot Q_2)/(2m_\mu^2))\end{aligned}$$

$$Q_3^2 = Q_1^2 + 2Q_1 \cdot Q_2 + Q_2^2$$
$$Q_1 \cdot Q_2 = Q_1 Q_2 \tau$$

$$P_i = \frac{1}{Q_i^2},\ i = 1, 2, 3$$

$$X(Q_1, Q_2, \tau) = \frac{1}{Q_1 Q_2 x} \arctan\left(\frac{zx}{1 - z\tau}\right)$$

$$x = \sqrt{1 - \tau^2}$$
$$z = \frac{Q_1 Q_2}{4m_\mu^2}(1 - R_{m1})(1 - R_{m2})$$

$$R_{mi} = \sqrt{1 + \frac{4m_\mu^2}{Q_i^2}},\ i = 1, 2$$

B.5.2 Form Factors

$$\mathcal{F}^{\text{LMD+V}}_{\pi^0\gamma^*\gamma^*}(q_1^2, q_2^2) = \frac{F_\pi}{3} \frac{q_1^2 q_2^2 (q_1^2 + q_2^2) + h_2 q_1^2 q_2^2 + h_5 (q_1^2 + q_2^2) + h_7}{(q_1^2 - M_{V_1}^2)(q_1^2 - M_{V_2}^2)(q_2^2 - M_{V_1}^2)(q_2^2 - M_{V_2}^2)}$$

$$\mathcal{F}_{Q^4}(-Q_1^2, -Q_2^2) = \sqrt{\frac{4\Gamma_{\pi^0 \to \gamma\gamma'}}{\pi\alpha^2 m_\pi^3}} \left[1 - a(Q_1^2 + Q_2^2) + b(Q_1^4 + Q_2^4) + cQ_1^2 Q_2^2 + \cdots\right]$$

$$\mathcal{F}_{Q^6}(-Q_1^2, -Q_2^2) = \sqrt{\frac{4\Gamma_{\pi^0 \to \gamma\gamma'}}{\pi\alpha^2 m_\pi^3}} \left[1 - a(Q_1^2 + Q_2^2) + b(Q_1^4 + Q_2^4) + cQ_1^2 Q_2^2 + d(Q_1^6 + Q_2^6) + e(Q_1^4 Q_2^2 + Q_1^2 Q_2^4) + \cdots\right]$$

B.6 Constants

Name	Symbol	Value	Units
Fine Structure Constant	α	0.0072973525693	-
Pion Mass	m_π	0.1349768	GeV/c^2
Muon Mass	m_μ	0.1056583745	GeV/c^2
Pion Decay Constant	F_π	0.0924	GeV
Vector Meson Mass 1	M_{V_1}	0.77549	GeV
Vector Meson Mass 2	M_{V_2}	1.465	GeV
LMD+V Parameter 1	h_2	-10.634883404844444	GeV^2
LMD+V Parameter 2	h_5	6.93	GeV^4
LMD+V Parameter 3	h_7	-14.827668978756119	GeV^6
TFF Expansion Param 1	a	1.6613939123981294*	GeV^{-2}
TFF Expansion Param 2	b	2.7619453491551749*	GeV^{-4}
TFF Expansion Param 3	c	3.259027816403921*	GeV^{-6}
TFF Expansion Param 4	d	-4.59258	GeV^{-6}
TFF Expansion Param 5	e	-5.58268	GeV^{-6}
?	Γ and $\Gamma_{\pi^0\to\gamma\gamma'}$	7.7291993×10^{-9}	GeV

$*$ - The values for the parameters a, b, and c in the table are approximate. Their exact forms are:

$$a = \frac{1}{M_{V_1}^2} + \frac{1}{M_{V_2}^2} + \frac{h_5}{h_7}$$

$$b = \frac{1}{M_{V_1}^4} + \frac{1}{M_{V_2}^4} + \frac{1}{M_{V_1}^2 M_{V_2}^2} + \frac{h_5}{h_7}\left(\frac{1}{M_{V_1}^2} + \frac{1}{M_{V_2}^2}\right)$$

$$c = \left(\frac{1}{M_{V_1}^2} + \frac{1}{M_{V_2}^2}\right)^2 + \frac{h_2}{h_7} + 2\frac{h_5}{h_7}\left(\frac{1}{M_{V_1}^2} + \frac{1}{M_{V_2}^2}\right)$$

C Radiative corrections

There are two types of radiative effects to consider in the $eA \rightarrow e'\pi^0 A$ reaction. The first is external radiation, which occurs when the incoming or outgoing electron radiates a bremsstrahlung photon when passing through the target. For external radiation the photon emission is incoherent with the electroproduction amplitude. External radiation can be modeled with GEANT, and this process has been turned on in our experiment simulation. The second type of radiative effect is internal radiation, where a photon is emitted from the incoming or outgoing electron coherently in the electroproduction amplitude. A third type of radiation is hadronic radiation, which is negligible in this reaction because the pion is neutral and the nuclear recoil momentum is extremely low.

C.1 Internal radiation in the experiment simulation

To model internal radiation in our simulation we utilized the approach given by Mo and Tsai [38], where the probability for internal radiation to occur from the incident or scattered electron is given by an effective internal radiator with length given by,

$$t_{initial} = t_{final} = \frac{3}{4}\frac{\alpha}{\pi}\left[ln\frac{Q^2 + 2m_e^2}{m_e^2} - 1\right] \tag{22}$$

This method provides a tractable approach for calculating acceptances and resolutions for proposal development, and was incorporated into our simulation.

For both external and internal radiation emitted photons are strongly peaked in the direction of the radiating electron, $\theta_\gamma \approx m_e/E_\gamma$. Because the experiment does not use a magnetic field to bend the scattered electron, energies of the scattered electron and photon radiated from the scattered electron are generally summed into the same energy cluster in HYCAL. Therefore, we expect the radiative effect for the scattered electron to be small compared to the radiative effect for the incident electron, where the radiated photon goes down the beam-line and is lost.

Our calculations show that the probability for internal radiation to occur is approximately 2 %, with 20 % of the photons generated having an energy greater than 1 MeV. Therefore, the probability for internal radiation to produce a photon with energy greater than 1 MeV is 0.4 %.

C.2 Applying radiative corrections to experimental yields

In this section we present the approach developed by S. Srednyak for the analysis of PRad data to correct experimental yields for radiative processes. Radiative corrections are dominated by real and virtual photon emission from the scattered electron, with the diagrams for these processes depicted in Fig 43. The phase space available for the real photon is dictated by the detector. In practice this means defining a 3d volume in the space of the

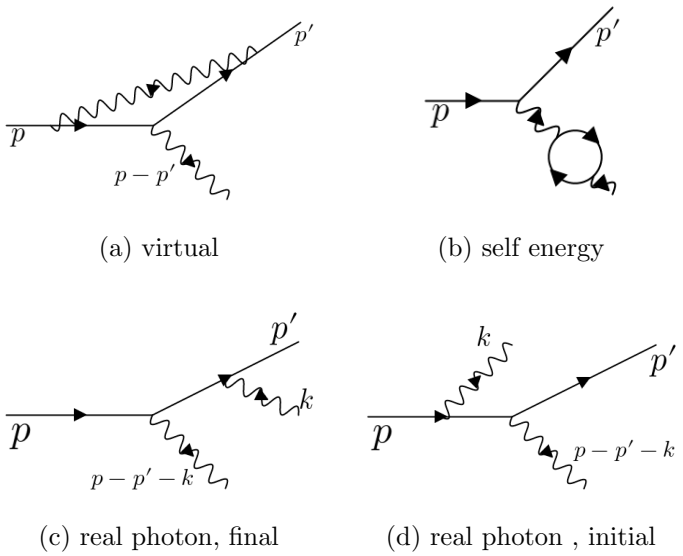

(a) virtual (b) self energy

(c) real photon, final (d) real photon , initial

Figure 43: Next to leading order radiative corrections are dominated by virtual photon emission in diagram (a), and real photon emission in diagrams (c) and (d).

real photon 3-momentum over which integration must be carried out. These volumes can be different for initial and final emission. These integrals are IR divergent and the IR divergence must be cancelled with the IR divergence that comes from the virtual part. The technique for such calculations has been developed over the years in papers by Akushevich , Ilyichev, and Shumeiko et.al. [39, 40]. We will apply these techniques to evaluate radiative corrections for the current experiment. There is a corresponding contribution to radiative corrections that comes from real photon emission from the hadronic part. This contribution is power suppressed by the hadronic mass scale, and is negligible compared to emission from the lepton.

In the following subsections we present details on the calculation of the Radiative Corrections(RCs). We will focus on the so-called model independent RCs that physically correspond to real photon emission from the scattered electron and corresponding virtual corrections. Diagrams for these processes are given in Fig.43. The calculation naturally splits into the calculation of the virtual and real parts.

C.2.1 Virtual Radiative corrections

This part is classical and has been considered in the context of anomalous magnetic moment computation. It was recently used for similar computations for SIDIS [41]. We have to

obtain expressions for the following integrals

$$I_{0,\mu,\mu\nu} = \int dl\{1, l_\mu, l_\mu l_\nu\} \frac{1}{l^2(l^2+2k_1l)(l^2+2k_2l)} \tag{23}$$

where k_1 are on mass shell. These integrals depend only on the single dimensionless kinematic variable $s = k_1k_2/m^2$ and the dimensional regularizatio parameter $\epsilon = d-4$. Using tensor decomposition, these integrals can be reduced to scalar 2-,3- point functions. We will focus here on the IR divergent contribution I_0.

Using Feynman parametrization, we obtain

$$I_0 = C(d) \int_0^1 dx \int_0^{1-x} dy(-\Delta^2)^\delta \tag{24}$$

with $\delta = -3 + d/2$,

$$C(d) = \pi^d \Gamma(3-d/2)\Gamma(\frac{d}{2}) \tag{25}$$

and

$$\Delta^2 = -(xk_1 + yk_2)^2 = -x^2m^2 + 2xyk_1k_2 - y^2m^2 \tag{26}$$

The k_i-dependent factor

$$I = \int_0^1 dx \int_0^{1-x} dy(-\Delta^2)^{d/2-3} = \int (-\Delta^2)^\delta dxdy \tag{27}$$

is IR divergent. We will need it only for special values of parameters

$$I = (m^2)^\delta \int (x^2+y^2-2sxy)^\delta dxdy \tag{28}$$

where

$$s = \frac{k_1k_2}{m^2} \tag{29}$$

We diagonalize the quadratic form by a linear transform

$$\begin{pmatrix} x \\ y \end{pmatrix} = S \begin{pmatrix} u \\ v \end{pmatrix} \tag{30}$$

where S is the square root of the matrix Q

$$Q = \begin{pmatrix} 1 & -s \\ -s & 1 \end{pmatrix} \tag{31}$$

$$Q = S^T S \tag{32}$$

(for general Q there are 4 solutions). There is a residual $SO(2,\mathbb{C})$ symmetry. We can use it to choose coordinates u, v such that the boundary of integration $x + y = 1$ takes the form $u = \rho$. This implies that the matrix S is of the form

$$S = \rho \begin{pmatrix} 1 & 1 \\ \mu & -\mu \end{pmatrix} \tag{33}$$

with

$$\rho^2 = \frac{1}{1+\mu^2} \tag{34}$$

and

$$\frac{1-\mu^2}{1+\mu^2} = s, \Rightarrow, \mu = \sqrt{\frac{1-s}{1+s}} \tag{35}$$

Then

$$I = \frac{1}{\rho^2 \mu}(m^2)^\delta \int_0^\rho du \int_{-\mu u}^{+\mu u} dv (u^2+v^2)^\delta \tag{36}$$

which gives

$$I = \frac{1}{\rho^2 \mu}(-m^2)^\delta \frac{\rho^{2\delta+2}}{2\delta+2} 2 \int_0^\mu dz (1+z^2)^\delta \tag{37}$$

The divergent part of this expression equals

$$I_{div} = \frac{1}{\rho^2 \mu}(m^2)^{-1} \frac{1}{2\delta+2} 2 \int_0^\mu dz (z^2+1)^{-1} \tag{38}$$

This must cancel with IR divergence from bremsstrahlung.

$$I_{div} = \frac{1}{\rho^2 \mu}(m^2)^{-1} \frac{1}{2\delta+2}(-i) log \frac{i+\mu}{i-\mu} \tag{39}$$

This gives

$$I_{div} = \frac{1}{\rho^2 \mu}(m^2)^{-1} \frac{1}{2\delta+2}(-i) log \frac{i+\mu}{i-\mu} \tag{40}$$

Substituting μ gives

$$I_{div} = \frac{1}{\rho^2 \mu}(m^2)^{-1} \frac{1}{2\delta+2}(i) log[s + \sqrt{s^2-1}] \tag{41}$$

$$I_{div} = \frac{2}{\sqrt{s^2-1}}(m^2)^{-1} \frac{1}{2\delta+2} log[s + \sqrt{s^2-1}] \tag{42}$$

This cancels IR divergence in the real emission part.

C.2.2 Real emission.

The real emission was considered in a number of papers [42, 39, 43, 44] . It involves evaluation of the following integral

$$J = \int d^{d-1} l \frac{1}{l_0} \frac{1}{lk_1} \frac{1}{lk_2} \tag{43}$$

This integral was considered in a number of papers [39, 43]. There are some questions that have not been addressed in the literature. In particular, although the expression for finite part is known and expressible through dilogarithms, it is not known

- How the different branches of the dilogarithms are related after analytic continuation in parameters, i.e., what is the representation of the fundamental group of the complement in the flat bundle defined by the integral. Proper formalism should be developed along the lines of [45] and should be phrased using motivic fundamental group.
- There is no comparison with the approach in mathematical literature [46] that relies on hyperfunctions.
- Geometric meaning of the argument in [47] is not clarified. It must be related to the Aomoto divisor.

The lack of answers to these mathematical questions does not prevent us from obtaining numerical results, as we now demonstrate.

$$J = R^{d-4}/(d-4) \int d^{d-2} n \frac{1}{(k_{1,0} - k_1 n)(k_{2,0} - k_2 n)} \tag{44}$$

where integration is over (d-2) sphere.

$$J = R^{d-4}/(d-4) \int d^2 s (1-s^2)^{d-4} \frac{1}{(k_{1,0} - k_1 s)(k_{2,0} - k_2 s)} \tag{45}$$

where now integration is over the unit disk.

We can normalize it

$$J = R^{d-4}/(d-4) \int_{-1}^{1} d^2 s (1-s^2)^{d-4} \frac{1}{(k_{1,0} - k_1 s)(k_{2,0} - k_2 s)} \tag{46}$$

The IR divergent part can be shown to cancel with the IR divergent part from virtual correction [].

We are interested in the IR finite part, that is given by the derivative

$$I = \int d^2 s l n (1-s^2) \frac{1}{(k_{1,0} - k_1 s)(k_{2,0} - k_2 s)} \tag{47}$$

We will consider normalized version

$$I = \int d^2 s ln(1-s^2) \frac{1}{(1-n_1 s)(1-n_2 s)} \tag{48}$$

with n_i Euclidean and $n_i^2 < 1$. After Feynman parametrization, we obtain

$$I = \int_0^1 dx \int d^2 s ln(1-s^2) \frac{1}{(1-ns)^2} \tag{49}$$

where

$$n = x n_1 + (1-x) n_2 \tag{50}$$

Then, after integrating over the angle,

$$I = 2\pi \int_0^1 dx \int_0^1 r dr ln(1-r^2) \frac{2\pi}{(1-n^2 r^2)^{3/2}} \tag{51}$$

$$I = 2\pi \int_0^1 dx \frac{1}{n^2 \sqrt{1-n^2}} [ln \frac{1+\sqrt{1-n^2}}{1-\sqrt{1-n^2}} - \tag{52}$$

$$-2ln(2) + ln \frac{n^2}{1-n^2}] \tag{53}$$

One can either proceed numerically or as in [39, 47] to obtain analytic expression.

References

[1] I. Larin et al. Precision measurement of the neutral pion lifetime. *Science*, 368:5064–509, 2020.

[2] PRad Collaboration. https://userweb.jlab.orgm̃ezianem/PRAD/PCR_PAC38_final.pdf.

[3] C.F. Redmer (BESIII Collaboration). *13th Conference on the Intersections of Particle and Nuclear Physics*, 2018.

[4] H. J. Behrend et al. (CELLO Collaboration). *Z. Phys. C*, 49:401, 1991.

[5] J. Gronberg et al.(CLEO Collaboration). *Phys. Rev. D*, 57:33, 1998.

[6] Lazzeroni et al. *Phys. Lett. B*, 768:38, 2017.

[7] P. Adlarson (A2 Collaboration). *Phys. Rev. C*, 95:035208, 2017.

[8] R. Akhmetshin (CMD-2 Collaboration). *Phys. Lett. B*, 605:26, 2005.

[9] M. Achasov et al. *Phys. Lett. B*, 559:171, 2003.

[10] M. Achasov et al.(SND Collabortion). *Phys. Rev. D*, 93:092001, 2016.

[11] M. Achasov et al. *Phys. Rev. D*, 98:112001, 2018.

[12] A. M. Bernstein and B. R. Holstein. *Rev. Mod. Phys.*, 85:49, 2013.

[13] M. Vanderhaeghen I. Danilkin, C.F. Redmer. The hadronic light-by-light contribution to the muon's amomalous magnetic moment. *Prog. Part. Nucl. Phys.*, 107:20, 2019.

[14] T. Aoyama et al. The anomalous magnetic moment of the muon in the Standard Model. *Phys. Rep.*, 887:1, 2020.

[15] E. Hadjimichael and S. Fallieros. *Phys. Rev. C*, 39:1438, 1989.

[16] T.W. Donnelly and S.R. Cotanch. *Proceedings of the 1985 CEBAF Summer Study*, 1985.

[17] A. Bramon J. Bijnens and F. Cornet. *Phys. Rev. Lett.*, 61:1453, 1988.

[18] B. Moussallam. *Phys. Rev. D*, 51:4939, 1995.

[19] A. Bramon J. Bijnens and F. Cornet. *Z. Phys. C*, 46:599, 1990.

[20] L.G. Landsberg. *Phys. Rep.*, 128:302, 1985.

[21] P. Maris and P.C. Tandy. *Nuclear Physics A*, 663 & 664:401c, 2000.

[22] M.R. Frank et al. *Phys. Lett. B*, 359:17, 1995.

[23] T. Blum et al. Hadronic Light-by-Light Scattering Contribution to the Muon Anomalous Magnetic Moment from Lattice QCD. *Phys. Rev. Lett.*, 124:132002, 2020.

[24] En-Hung Chao et al. Hadronic light-by-light contribution to $(g-2)_\mu$ from lattice QCD: a complete calculation. *EPJC*, 81:651, 2021.

[25] *The Science Driving the 12 GeV Upgrade of CEBAF, https://www.jlab.org/div dept/physics division/GeV/WhitePaper V11.pdf*, 2001.

[26] *Conceptual Design Report (CDR) for the Science and Experimental Equipment for the 12 GeV Upgrade of CEBAF, https://www.jlab.org/div dept/physics division/GeV/doe_review/CDR for Science Review.pdf*, 2005.

[27] B. Abi et al. Measurement of the Positive Muon Anomalous Magnetic Moment to 0.46 ppm. *Phys. Rev. Lett.*, 126:141801, 2021.

[28] A. Nyffeler. Precision of a data-driven estimate of hadronic light-by-light scattering in the muon g-2: Pseudoscalar-pole contribution. *Phys. Rev. D*, 94:053006, 2016.

[29] S. Gevorkyan, I. Larin, R. Miskimen, and E. Smith. Photoproduction of pion pairs at high energy and small angles. *[arXiv:2201.09923 [nucl-th]]*, 1 2022.

[30] Fan Yang et al. *J. Phys.: Conf. Ser.*, 404:012025, 2012.

[31] S. Fegan et al. Assessing the performance under ionizing radiation of lead tungstate scintillators for EM calorimetry in the CLAS12 Forward Tagger. *NIM*, A789:101, 2015.

[32] S. Boyarinov. Private communications.

[33] I.Larin, A.Gasparian, S.Gevorkyan, L.Gan. The π^0 background from ω and ρ,mesons photoproduction in PrimEx. *PrimEx-II experiment note #51, https://www.jlab.org/primex/primex_notes/omega_note.pdf*, 2007.

[34] T. J. Brodbeck, P. Coddington, J. V. Morris, D. Newton, and T. Sloan. Photoproduction of omega Mesons from Complex Nuclei Targets. *Nucl. Phys. B*, 136:95–114, 1978.

[35] G. Faldt. *Phys. Rev. C*, 86:024611, 2012.

[36] C. W. Akerlof, W. W. Ash, K. Berkelman, C. A. Lichtenstein, A. Ramanauskas, and R. H. Siemann. Measurement of the Pion Form Factor. *Phys. Rev.*, 163:1482–1497, 1967.

[37] S.Gevorkyan et al. *Phys. Rev. C*, 80:055201, 2009.

[38] L.W. Mo and Y.S. Tsai. Radiative corrections to elastic and inelastic ep and μp scattering. *Reviews of Modern Physics*, 41:205, 1969.

[39] D. Yu. Bardin and N. M. Shumeiko. An Exact Calculation of the Lowest Order Electromagnetic Correction to the Elastic Scattering. *Nucl. Phys. B*, 127:242–258, 1977.

[40] I. Akushevich, H. Gao, A. Ilyichev, and M. Meziane. Radiative corrections beyond the ultra relativistic limit in unpolarized ep elastic and Møller scatterings for the PRad Experiment at Jefferson Laboratory. *Eur. Phys. J. A*, 51(1):1, 2015.

[41] Igor Akushevich and Alexander Ilyichev. Lowest order QED radiative effects in polarized SIDIS. *Phys. Rev. D*, 100(3):033005, 2019.

[42] Luke W. Mo and Yung-Su Tsai. Radiative Corrections to Elastic and Inelastic e p and mu p Scattering. *Rev. Mod. Phys.*, 41:205–235, 1969.

[43] G. Passarino and M. J. G. Veltman. One Loop Corrections for e+ e- Annihilation Into mu+ mu- in the Weinberg Model. *Nucl. Phys. B*, 160:151–207, 1979.

[44] L. C. Maximon and J. A. Tjon. Radiative corrections to electron proton scattering. *Phys. Rev. C*, 62:054320, 2000.

[45] AA Beilinson, Alexander B Goncharov, VV Schechtman, and AN Varchenko. Aomoto dilogarithms, mixed hodge structures and motivic cohomology of pairs of triangles on the plane. In *The Grothendieck Festschrift*, pages 135–172. Springer, 2007.

[46] Kazuhiko Aomoto. Gauss-manin connections of schläfli type for hypersphere arrangements. In *Annales de l'institut Fourier*, volume 53, pages 977–995, 2003.

[47] A. Afanasev and A. Ilyichev. Radiative corrections to the lepton current in unpolarized elastic lp-interaction for fixed Q^2 and scattering angle. *Eur. Phys. J. A*, 57(9):280, 2021.